Dissertation Proposal

Nikhil Patten[1]

[1] *University of Wyoming*
1000 E University Avenue
Laramie, WY 82071, USA

(Dated: Spring 2024)

Contents

1. CHAPTER 1

1.1. *Introduction*

In the northern hemisphere, under a dark sky, one might be fortunate enough to witness the natural phenomenon known as the northern lights. These lights are notoriously difficult to track down as they are transient events that are not reliably predicted. One night they could be on full display while on another night they might be inexplicably absent. As well-known as these awe-inspiring displays of red and green streams that make up the northern lights are, their cause has been a mystery throughout most of human history. Ancient peoples across the globe have pondered this natural majestic spectacle, both in the northern hemisphere with the Aurora Borealis, as well as in the southern hemisphere with the Aurora Australis. In Scandinavia, aurorae were thought to foretell the death of kings. The earliest recordings of aurorae might very well be the Cro-Magnon cave paintings in Spain, dating back as far as 30,000 years ago (Eather 1980)!

Figure 1. The Aurora Australis as seen from the *ISS*. Image credit: *ESA*.

Curious onlookers are typically surprised to learn that the northern lights are the result of mass-loss from the Sun. Because of the Sun's dynamic magnetic field, streams of charged particles from the Solar corona are often ejected out into interplanetary space. If the Earth is in the way of this "Solar wind," this stream of charged protons and electrons spiral into the Earth's magnetic poles and excite atoms in the atmosphere to create these famous lights as the charged Solar particles collisionally excite ions in the Earth's upper atmosphere. Figure 1 shows the Aurora Australis from the International Space Station (*ISS*). The different-colored luminescence indicate electron transitions in different atomic-species in the Earth's atmosphere with red at high altitudes corresponding to Oxygen transitions, and lower-latitude transitions of Oxygen green and Nitrogen blue/purple/red

(Eather 1980). The rarefied air in the Earth's upper-atmosphere allows for these "forbidden" transitions to be on full-display, whereas they are usually extinguished in higher-pressure environments before these transitions can occur. Figure 1 shows this effect on full-display, with different transitions displayed at different heights in the Earth's atmosphere, demonstrating the different conditions required for each transition.

1.1.1. *Stellar mass loss*

Stars below the Kraft break ($T_{\rm eff} \lesssim 6200$ K) are known to exhibit magnetic activity as a result of their convective envelopes (Schatzman 1962; Kraft 1967). With this magnetic activity come phenomena such as magnetic breaking, coronal mass ejections (CMEs), and solar winds during the main sequence. For a Sun-like star (spectral type G2V), mass loss through solar winds is of the order $\dot{M} \approx 10^{-12}\ M_\odot\ {\rm yr}^{-1}$(Airapetian & Usmanov 2016). For the time on the main-sequence, $\tau_{\rm MS} \approx 10^{10}$ years, this represents a decrease in mass on the order of $10^{-2}\ M_\odot$. This slight change in mass on the main-sequence is not enough to seriously alter the evolutionary path of a main-sequence star (Willson 2000).

Sub-Solar to intermediate mass stars ($0.5 \lesssim M/M_\odot \lesssim 8.0$) experience significant mass loss at the end of the main sequence. After their time on the main sequence, these stars migrate through the asymptotic giant branch (AGB). In this stage of evolution, the star experiences period "flashes" as hydrogen shell burning dumps helium ash causing "flashes" of helium shell burning. These long period thermal pulses expel the outer layers of the star and can expel as much as $10^{-4}\ M_\odot\ {\rm yr}^{-1}$ Vassiliadis & Wood (1993).

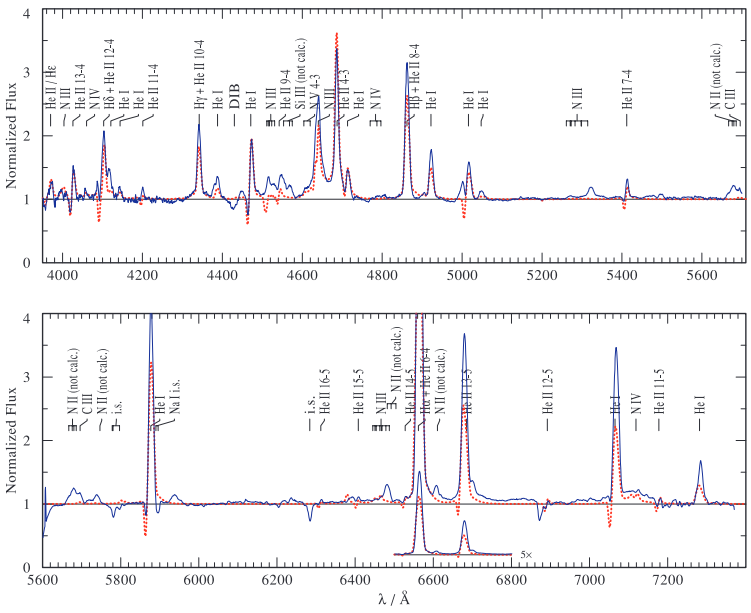

Figure 2. Normalized spectrum of a WN star (see Figure 3 of Gvaramadze et al. 2009)

Massive stars also display mass loss. In later stages of stellar evolution, massive stars ($M/M_\odot \gtrsim 8.0$) can evolve into Luminous Blue Variables (LBVs) and Wolf-Rayet (WR) stars. During an instability-driven pulsation, a LBV can shed $\sim 1\ M_\odot$ in one pulsation (Humphreys & Davidson 1994)! Figure 2 presents a spectrum of a Wolf-Rayet star from the work of Gvaramadze et al. (2009).

This WR star has strong He I, He II, H, and N emission lines. A WR star is a stage of post-main-sequence evolution in which the nuclear-processed material is brought to the surface through mixing. Mixing is demonstrated in the spectrum shown in Figure 2 by the strong nitrogen emission lines. Metals brought to the surface result in a "heavier" wind in which mass-loss rates are of the order $10^{-5}\ M_\odot\ \mathrm{yr}^{-1}$ (Crowther 2007). In a similar fashion to mass loss in WR stars, massive stars also continually lose mass while on the main-sequence through their winds. Because of the absence of magnetic activity in these stars, the fundamental mechanism of mass loss is different for massive stars when compared to Solar-type stars.

1.1.2. *Wind driven mass loss*

Massive stars were suspected to exhibit wind-driven mass loss long before observational data for these objects were available. Milne (1926) was the first to posit that radiative acceleration might be able to overcome gravitational acceleration for the most luminous stars. Castor, Abbott, and Klein, often abbreviated as CAK, expanded upon this idea in their seminal 1975 paper (Castor et al. 1975). The work of Castor et al. (1975) is fundamental because they were the first to quantitatively estimate mass loss for O and B stars on the main sequence by considering the sum of the strengths of all ion transition lines in a star's atmosphere. This would imply an expanding atmosphere that would lose mass as a function of effective temperature of the star. Castor et al. (1975) predicted that an O5 main-sequence star would lose up to $10^{-6}\ M_\odot\ \mathrm{yr}^{-1}$. Even considering the shorter lifetimes of OB stars compared to Solar-type stars, $\dot{M} = 10^{-6}\ M_\odot\ \mathrm{yr}^{-1}$ represents a significant reduction in mass during the main-sequence phase of the star. For an O5V star, this corresponds to losing as much as one-fourth to one-third its total mass during the main sequence alone. They also note the possibility of nuclear-processed material being exposed for some of these stars as a result of violently losing its outer layers.

One consequence of this mechanism of winds from massive stars is that the strength of the wind, and thus the magnitude of mass loss, would be dependent on the metallicity of the star. Since there are fewer UV transitions for H I and He I compared to metal ions, we expect the majority of the line acceleration to come from C, N, O, and Fe transitions. Higher metallicity stars should exhibit larger mass loss than metal-poor stars.

Another important consideration is the ionization state of the metal ions that drive the wind. Changes in the ionization state of the wind-driving ions can have severe implications for the wind strength. If the ionization state of an ion decrements, more transitions become available in the UV which increases the metal-line opacity overall (Pauldrach et al. 1990; Lamers et al. 1995). This effect is predicted to cause a sharp increase in the mass-loss rates for stars cooler than $T_{\mathrm{eff}} \lesssim 21,000$ K, due to the transition of Fe IV to Fe III. This predicted drastic change in mass loss over a small range of T_{eff} is known as the "bistability jump" (Pauldrach et al. 1990).

Using the work of Castor et al. (1975), predictions for mass-loss rates as a function of stellar parameters have been developed. Vink et al. (2001) released the most prolific set of predictions covering a larger temperature range of $12,500 \leq T_{\mathrm{eff}} \leq 50,000$ K. Because of the consequences of the bi-stability jump, the mass loss predictions are separated into two regimes—on the hot and cool sides of $\sim$21,000 K. Vink et al. (2001) parameterized mass loss as function of stellar parameters (luminosity L_*, mass M_*, terminal wind speed v_∞, temperature T_{eff}, and metallicity Z) on the hot side as,

$$
\begin{aligned}
\log \dot{M} = & -6.697 \\
& +2.194 \log \left(L_*/10^5\right) \\
& -1.313 \log \left(M_*/30\right) \\
& -1.226 \log \left(\frac{v_\infty/v_{\rm esc}}{2.0}\right) \\
& +0.933 \log \left(T_{\rm eff}/40,000\right) \\
& -10.92 \left[\log \left(T_{\rm eff}/40,000\right)\right]^2 \\
& +0.85 \log \left(Z/Z_\odot\right) \ ,
\end{aligned}
$$

and on the cool side as,

$$
\begin{aligned}
\log \dot{M} = & -6.688 \\
& +2.210 \log \left(L_*/10^5\right) \\
& -1.339 \log \left(M_*/30\right) \\
& -1.601 \log \left(\frac{v_\infty/v_{\rm esc}}{2.0}\right) \\
& +1.07 \log \left(T_{\rm eff}/20,000\right) \\
& +0.85 \log \left(Z/Z_\odot\right) \ .
\end{aligned}
$$

Although widely used in literature, the predictions of Vink et al. (2001) have been criticized for over-predicting mass loss in certain regimes. As such, others have set out to revise the set of predictions for mass-loss rates. Lucy (2010) presented a set of predictions for mid- to late-O stars. These predictions covered a temperature range of $27,500 \leq T_{\rm eff} \leq 40,000$ K and gravity range of $3.25 \leq \log g \leq 4.25$. Krtička (2014) also released a set of models covering the regime of B main-sequence stars, with the hottest stars having a mass-loss rate of 10^{-9} $M_\odot$ yr^{-1}. This represents a reduction in the mass-loss rates of Vink et al. (2001) by factors of several. Updated prescriptions also take into account factors such as rotation and more-sophisticated metallicity dependence (Gormaz-Matamala et al. 2023, 2022).

1.2. *Relevance to Astrophysics*

The life and death of OB stars are intertwined with many subfields of astronomy. During their lifetimes on the main-sequence, OB stars are the source of powerful winds that shape and alter their local environments. Massive stars are the driving mechanism for enriching the ISM of their host galaxies. Massive stars also inject energy into their surrounding environment through UV radiation and high-momentum stellar winds in a process referred to as "feedback." This stellar feedback can sweep-up surrounding gas and form dense filaments, triggering new star formation (Elmegreen & Lada 1977). Massive stars therefore can have a significant impact on star formation and evolution on the host galaxy as a whole (van der Kruit & Freeman 2011). Small differences in mass-loss rates can have profound implications for stellar-evolution. For example, differences in mass-loss rates of a factor of 2 can be the determining factor in the star's evolution and end state Meynet et al. (1994).

How the mass of a hot and luminous star changes throughout its lifetime has profound implications for the formation of degenerate objects—white dwarfs and neutron stars—as well as black holes. The formation of these compact objects is of growing importance with detailed study of the evolution and fate of compact objects in binaries (Abbott et al. 2017a,b, 2019).

1.3. *Measuring mass-loss rates*

Kudritzki & Puls (2000) and Puls et al. (2008) reviewed techniques used to estimate mass-loss rates from winds of hot stars. The three canonical observational techniques are Hα recombination lines, thermal radio/FIR continuum emission (the two so-called "density-squared diagnostics"), and UV resonance lines. Different techniques are useful in different stellar temperature and mass-loss rate regimes while also suffering from their own individual limitations and systematic sources of uncertainty.

1.3.1. *Hα recombination lines and thermal radio/FIR continuum emission*

Hα recombination lines have widely been used to measure mass loss from late-O and early-B stars. The idea goes back to the works Klein & Castor (1978), Leitherer (1988) and relies on tracing Hα emission, originating in the wind, to infer a density of the wind. Combining this knowledge with information about the velocity profile of the wind allows for an estimation of the mass lost through the wind. In the limit of the most luminous stars with heavy mass loss, Hα emission in the wind is optically thick, making it easy to disentangle the emission component of Hα from the stellar photospheric absorption and measure mass loss. Another advantage is that this technique requires Hα spectroscopy, which can be performed from the ground and does not require space-based observations.

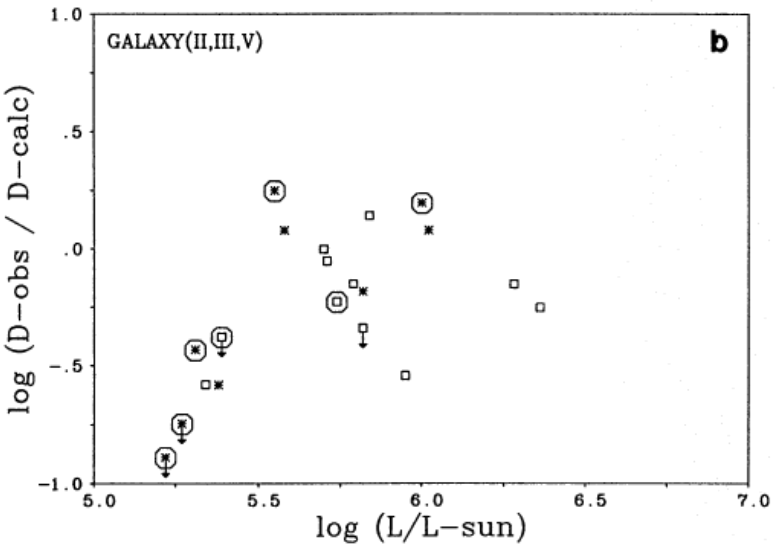

Figure 3. Difference between the results of Hα measurements and the theoretical predictions as a function of stellar luminosity (see Figure 26b of Puls et al. 1996).

Hα recombination is a density-squared (n^2) diagnostic, meaning the excess flux in Hα scales as physical density of the wind squared. The result of this dependency is that small variations in the

density of the stellar wind can have large impacts on mass-loss rates produced by this method. This caveat can be problematic for OB stars as they are known to exhibit variability and display density inhomogeneities in their winds (Owocki et al. 1988; Feldmeier 1995; Dessart & Owocki 2005). Another confounding factor is disentangling the Hα emission and absorption with the nearby absorption feature He II λ6560. Some lines in the Pickering series of singly ionized helium almost overlap with the Balmer series for neutral hydrogen (Plaskett 1922). Instrumental and pressure broadening can blend these features together, thus requiring precise atmospheric modelling to isolate Hα emission from the wind. Lastly, another limitation of this technique is its applicability. Since Hα recombination is dependent on the density of the stellar outflow, this technique is limited to the regime of O- and B-stars with "strong" winds. At lower wind densities, corresponding to $\dot{M} \lesssim 10^{-8}\ M_{\odot}\ \mathrm{yr}^{-1}$, H$\alpha$ emission becomes insignificant relative to the photospheric Hα absorption (Puls et al. 2008), necessitating other methods.

The Hα spectroscopic technique has been applied many times since its inception (Leitherer 1988; Drew 1990; Lamers & Leitherer 1993; Puls et al. 1996; Markova et al. 2004). Puls et al. (1996) studied 24 luminous Galactic O stars. Figure 3 plots the difference between mass-loss rates reported by Puls et al. (1996) and theoretical predictions as a function of luminosity for their Galactic sample. On the y-axis, D, is directly proportional to the mass-loss rate, $\dot{M}$. Less luminous objects display a systematic discrepancy between observations and theory, with measurements being lower than theoretical predictions. There is large scatter in the residuals for $L \gtrsim 10^{5.25}\ L_{\odot}$. Markova et al. (2004) studied a set of 29 Galactic O-stars solely using Hα analysis, following the approach developed by Puls et al. (1996). They found mass-loss rates ranging from $0.3--16 \times 10^{-6}\ M_{\odot}\ \mathrm{yr}^{-1}$ (Markova et al. 2004). Their analysis was limited to early O stars and late O supergiants—luminous early-type stars. This selection again reflects the limitation on the applicability of Hα techniques. In their analysis, Markova et al. (2004) found systematic scatter in comparison to other Hα results. Markova et al. (2004) were however, able to demonstrate agreement between Hα- and radio-derived mass-loss rates.

The thermal-radio/FIR continuum approach was independently developed by Wright & Barlow (1975) and Panagia & Felli (1975). Instead of using optical bandpasses, this method searches at longer wavelengths for signatures of stellar outflow. The basic idea is to use excess flux—the difference between the observed intensity and that predicted by stellar atmosphere models at longer wavelengths—as an indicator of mass loss in the wind. At far-IR and radio wavelengths, the star itself emits nearly zero flux, meaning that all the flux in far-IR and radio regimes arise from emission due to free-free and free-bound processes in the wind.

The thermal radio/FIR method is also an n^2 diagnostic, and as such, suffers from the limitations of Hα. Radio and FIR techniques are only sensitive to larger wind densities, when excess flux is easily detectable. Some of the early work utilizing this method was conducted by Abbott et al. (1980). They studied 15 O and early-B stars using VLA radio measurements. Abbott et al. (1980) found mass-loss rates ranging between 2.5×10^{-7}–$2.5 \times 10^{-5}\ M_{\odot}\ \mathrm{yr}^{-1}$ and demonstrated agreement between radio-derived mass-loss rates and other techniques to within a factor of 3. Even in their small sample size however, one star, 9 Sgr, showed deviations from other techniques by over an order of magnitude.

1.3.2. *UV resonance lines*

The analysis of UV lines as a means to measure mass loss was first suggested by Hamann (1981) and Lamers et al. (1987). By analyzing the P-Cygni profiles displayed in metal resonance

lines (C IV and N V in early-O stars and Si IV in late-O supergiants, for example), information about the stellar wind can be extracted. UV analysis samples regions near the star, all the way out to the tenuous outer reaches of the wind. The difference between the blue absorption and red emission components of the P-Cygni profile gives the maximum wind speed, v_∞. Analyzing the depths of the metal-resonance features, and using typical scaling relations, a density of the out-flowing stellar wind can be measured and, combining this with a velocity profile of the wind, the mass-loss rate becomes measurable.

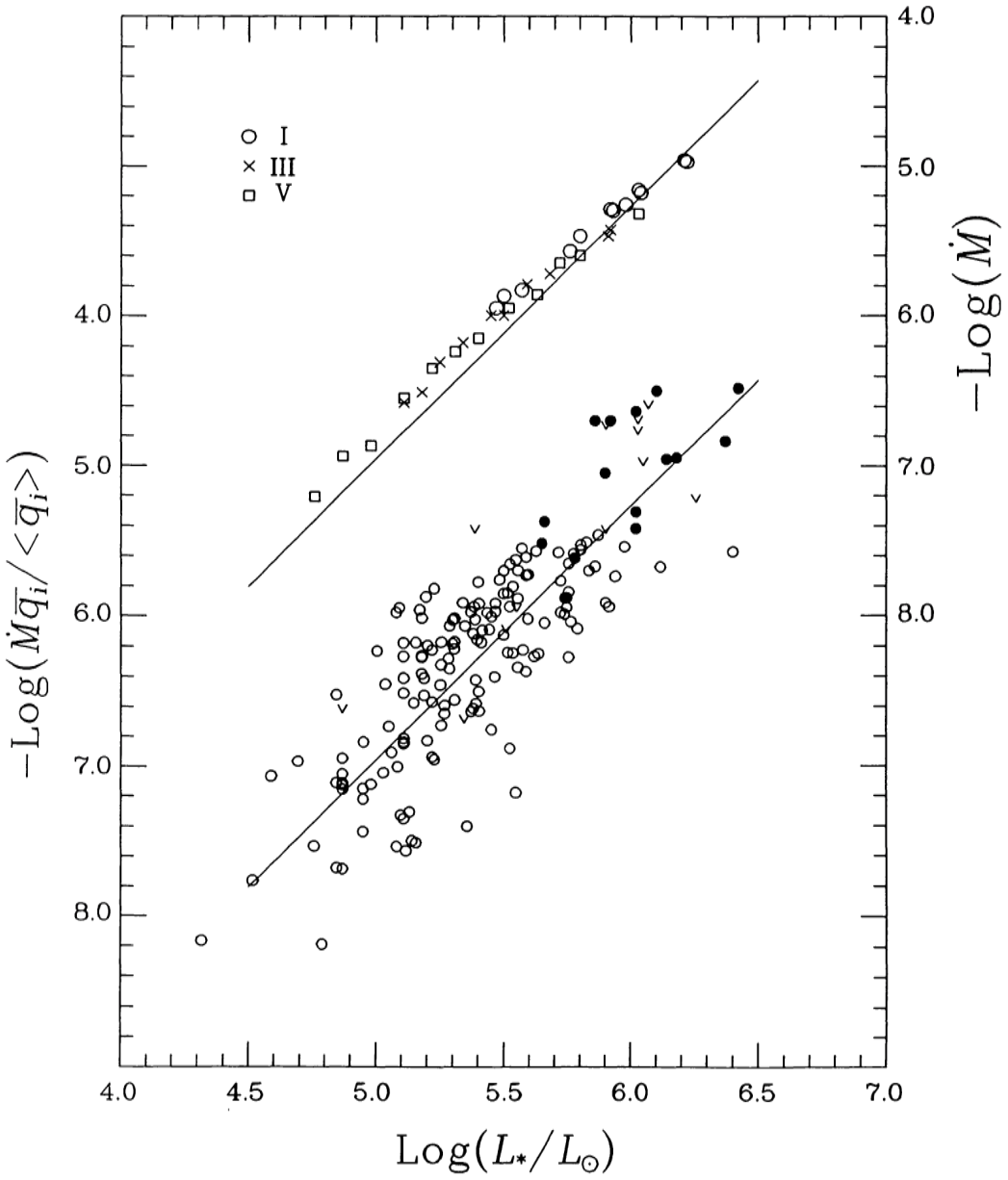

Figure 4. Mass-loss rate as a function of luminosity from UV-based methods (see Figure 15 of Howarth & Prinja 1989).

The drawback of this method is that metal resonance lines are rarely unsaturated under typical conditions. UV diagnostics, therefore, often provide a lower-limit to $\dot{M}$, rather than an accurate measurement. In addition to saturation, metal resonance lines also commonly display extended regions in the absorption component of the profile with almost zero intensity, referred to as "black troughs," (see Puls et al. 1993; Hamann 1981, for more detail). The presence of these black troughs only complicates the analysis, and necessitates more assumptions about the wind. Because of these complications, UV measurements typically underestimate mass-loss rates.

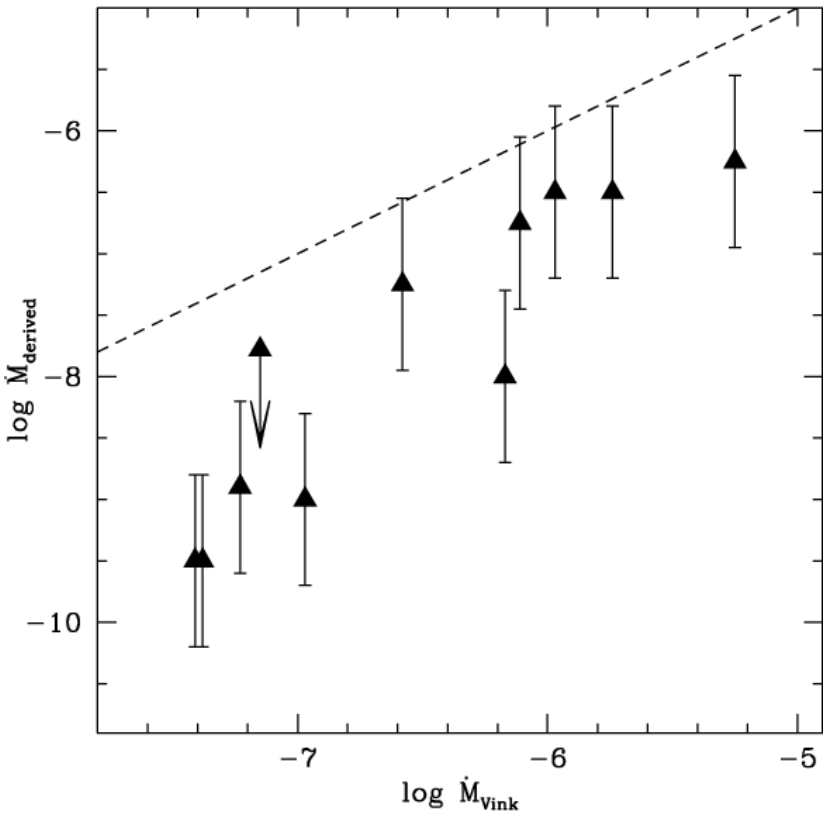

Figure 5. UV-derived mass loss rates plotted against Vink et al. (2001) predictions (Figure 40 from Martins et al. 2005).

Many observational studies (Garmany et al. 1981; Howarth & Prinja 1989; Martins et al. 2005; Fullerton et al. 2006; Marcolino et al. 2009) have used UV spectra, primarily from the International Ultraviolet Explorer (IUE) and the Far Ultraviolet Spectroscopic Explorer (FUSE), to measure wind profiles and determine v_∞ in deriving mass loss rates for early- to late-O stars. For example, Howarth & Prinja (1989) studied 203 Galactic O dwarfs, giants, and supergiants using the IUE. From their sample, they find mass-loss rates, $\log \dot{M}$, ranging from -5 to -8 in units of $M_\odot$ yr^{-1}. Figure 4 shows the UV-derived mass-loss rates plotted as a function of luminosity. The filled black circles are results of radio-derived mass loss rates from other works (references for each measurement are tabulated in Appendix A of Howarth & Prinja 1989). Circles indicate supergiants, x's mark giants, and squares designate dwarfs. The bottom line plots the results of UV measurements and corresponds to the left-hand axis. The top line plots the results of model, with measurements indicated by the right-hand axis. A positive correlation between luminosity and mass-loss is found in all listed UV studies with

1–2 dex of scatter. Additional analysis of Martins et al. (2005) set out to measure the mass loss rates of weak-winded stars by selecting a set of Galactic O dwarfs known to exhibit weak-winds. Figure 5 plots their observed versus predicted Vink et al. (2001) mass loss rates. The dashed line marks the one-to-one relation. All of the points fall 1–2 dex below the line, indicating systematic differences between measurements and theoretical expectations. This discrepancy becomes noticeably worse on the left side of the panel, corresponding to late O dwarfs, which have small mass-loss rates.

Kudritzki & Puls (2000), in their review of the literature, detailed possible systematic uncertainties associated with UV techniques. Reasons for the discrepancy is still an active area of work. The divergence of UV results and predictions, particularly at low $\dot{M}$, gives rise to what is known as the "weak wind problem." Weak-winded late-O dwarfs, studied in Marcolino et al. (2009), and extended to O giants by de Almeida et al. (2019), demonstrably show weaker UV-derived mass loss rates than predictions. One possible explanation of the weak-wind problem is small scale density inhomogeneities in the wind, or clumping. Currently, optically thin clumps are assumed when generating empirical predictions. Accounting for clumping could necessitate a reduction in mass-loss predictions or increase the mass-loss rates derived from observations for certain wind conditions (Sundqvist et al. 2011). Another possible solution to the weak-wind problem is that components of the stellar wind may be hidden in a hard-to-observe, highly ionized phase that is only detectable in X-rays. Huenemoerder et al. (2012) measured a hot massive wind in the X-rays of a O9.5V star, μ Columbae, that was previously classified as being weak-winded from UV studies.

For the O9.5V dwarf star ζ Oph, Abbott et al. (1980) measured a $\log \dot{M} = -6.42$, while the standard Vink et al. (2001) prediction yields a $\log \dot{M} = -6.89$, a discrepancy of 0.47 dex. Marcolino et al. (2009) report a value of $\log \dot{M} - 8.80$ using UV techniques. In light of these comparisons, the Abbott et al. (1980) result is regarded as an overestimate and the Marcolino et al. (2009) result as an underestimate.

1.4. *Using bowshock nebulae to measure mass-loss rates*

van Buren & McCray (1988) examined Infrared Astronomical Satellite (IRAS) images, and they reported the detection of extended arc- and ring-shaped structures as seen in infrared 60 and 100 μm bandpasses. They associated these nebulae with hot and luminous stars, classifying arcuate structures as stellar wind bowshocks—infrared emission from interstellar material swept up and compressed into an arc-shaped shock front by the stellar wind of a high-velocity massive star. The shock front, visible at 60 μm, is formed as a result of the collision of a stellar wind from a star moving supersonically with ambient material (van Buren & McCray 1988). Bowshock nebulae are most commonly associated with runaway hot and luminous stars, but have also been shown to originate around other types of energetic objects such as pulsars (Hartigan et al. 1987; Helfand et al. 2001; Wang et al. 2013), X-ray binaries (Gvaramadze et al. 2011), and evolved stars (Noriega-Crespo et al. 1997a; Gvaramadze et al. 2014a,b). van Buren & McCray (1988) listed 15 such objects, 13 of which being classified as stellar bowshocks. By mid 90's, van Buren et al. (1995) increased the census of bowshock nebulae to include 58 candidate stellar bowshocks based on the morphology (in spatially resolved cases) and or the presence of 60 μm excesses. Noriega-Crespo et al. (1997b) refined the list of van Buren et al. (1995) by using archival High resolution IRAS (HiRes) data to construct images of the 58 candidate objects. From this, Noriega-Crespo et al. (1997b) rejected three candidate objects and confirmed 6 new stellar bowshocks. Kobulnicky et al. (2016) conducted the most extensive search for stellar bowshocks by inspecting *Spitzer Space Telescope* (*SST*) and *Widefield Infrared Survey*

Explorer (*WISE*) mosaics and tabulated 709 candidate objects. Jayasinghe et al. (2019) added to this catalogue of bowshock candidates with the discovery of 311 new stellar bowshock candidates.

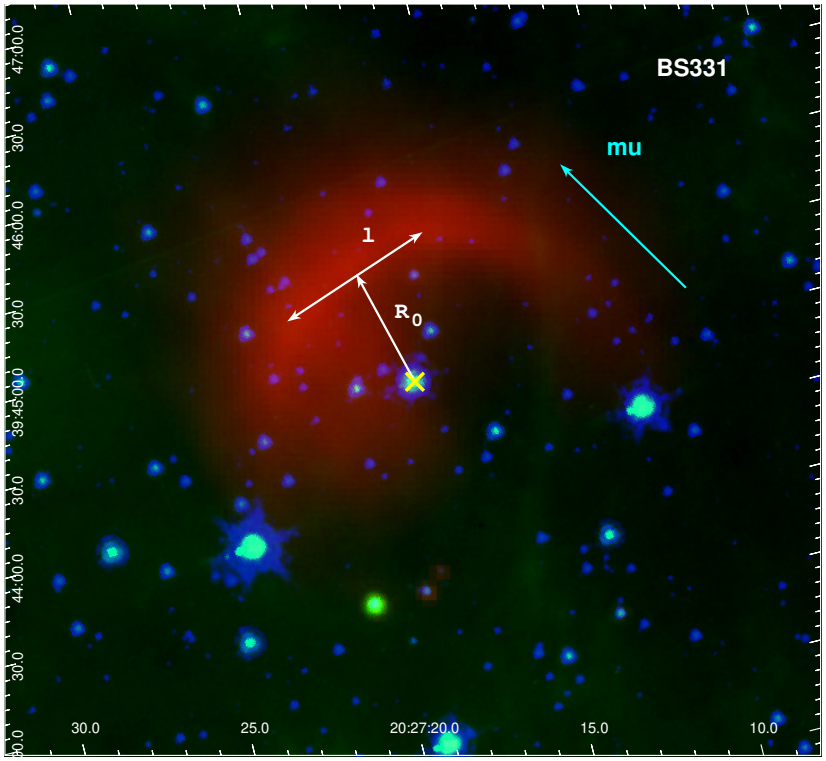

Figure 6. Three-color image of BS331 with red/green/blue representing 24/8.0/4.5 μm *SST* IR images.

Figure 6 shows a three-color representation of an archetypal bowshock nebula—denoted as Bowshock candidate 331 from the catalogue of Kobulnicky et al. (2016), with red/green/blue from *SST* 24/8.0/4.5 μm data. The arc-shaped shock front seen in 24 μm traces warm dust emission (Kobulnicky et al. 2010) and is the signature shape of bowshock nebulae. Green (8.0 μm data) encapsulates broad PAH emission and very hot dust near the star (Kobulnicky et al. 2016). Blue (4.5 μm data) is used for identification of stars (Kobulnicky et al. 2016). The yellow "X" marks the central star. The white arrow labeled "R_0" depicts the standoff distance—the distance from the central star to the shock front. The white arrow labeled "ℓ" is the distance running through the shock front perpendicular to the standoff distance and is known as the chord length. The cyan vector labeled "mu" shows the direction of the proper motion vector, as measured by Gaia in data release 3. The velocity vector of the central star is often aligned with the symmetry axis of the nebula because the bowshock is formed, in most instances, from the supersonic motion of a massive star relative to its surroundings.

The idea of using bowshock nebulae to measure mass loss was first proposed by Gull & Sofia (1979), in which the authors derived $\dot{M}$ for two stars powering bowshock nebulae. The authors suggested balancing the momentum flux from the mass lost through stellar wind with the pressure of the relative motion of the ambient ISM. Assuming rough estimates for values of the ambient density of the ISM and stellar terminal wind speeds, Gull & Sofia (1979) were able to generate estimates for the mass-loss rates for the O9.5V star ζ Oph and the K0 star LL Ori. For ζ Oph Gull & Sofia

(1979) reported a mass-loss rate of 2.3×10^{-8} $M_\odot$ yr^{-1}. This value is in excellent agreement with the results of Gvaramadze et al. (2012), who reported a mass-loss rate of 2.2×10^{-8} $M_\odot$ yr^{-1}. The Gull & Sofia (1979) result is also in decent agreement with the Vink et al. (2001) prediction of 1.3×10^{-7} $M_\odot$ yr^{-1}. For context, UV measurements from Marcolino et al. (2009) indicate a mass-loss rate of 1.58×10^{-9} $M_\odot$ yr^{-1}and Hα results from Puls et al. (1996) report a mass-loss rate of $\lesssim 3 \times 10^{-8}$

Using the principle of momentum balance first demonstrated in Gull & Sofia (1979), Kobulnicky et al. (2018) showed that mass-loss rate can be given as a function of four observable parameters: the velocity of the star, the terminal wind-speed of the star, the density of the ISM, and the standoff distance Using available multi-wavelength archival data, Kobulnicky et al. (2018) and Kobulnicky et al. (2019) combined all available spectral, proper motion, and infrared data to study the mass-loss rates for 20 and 70 bowshock central stars, respectively. The spectral types of the stars analyzed by Kobulnicky et al. (2019) ranged from O7–B5, sampling dwarfs, giants and supergiants in this temperature range. Derived mass-loss rates from Kobulnicky et al. (2019) range from 10^{-7} $M_\odot$ yr^{-1} for mid-O-dwarfs to 10^{-9} $M_\odot$ yr^{-1} for late-O-dwarfs. Kobulnicky et al. (2019) also found evidence for the predicted bi-stability gap, with an enhancement in mass-loss rate at $T_{\rm eff} \approx 22,000$ K.

1.4.1. *Stellar bowshock simulations*

Stellar bowshock nebulae typically form when winds from a high relative-velocity star collide with the surrounding ISM. Contrariwise, not all runaway stars produce bowshock nebulae, with recent studies finding bowshock nebulae around 5–15% of all runaway OB stars (Peri et al. 2015). The formation of a bowshock nebulae, as well as the morphology of the resultant nebulae can be expected to depend on several parameters; namely: wind speed; the density of the surrounding medium; the mass-flux of the stellar wind; and the relative velocity of the star with respect to the ambient ISM. The seminal work of Comeron & Kaper (1998) ran numerical simulations of runaway OB stars and synthesized how varying the previously itemized parameters affected the macroscopic properties of the stable stellar bowshock that formed.

Subsequent analysis investigated these trends further. Acreman et al. (2016) conducted a multiwavelength simulation of bowshock nebulae from runway early-type stars and convolved the resultant nebulae to typical instrumental beam-sizes and different viewing angles. Curiously, Acreman et al. (2016) found that the effects observed bowshock nebulae yield similar R_0 values

1.4.2. *Mass-loss rate equation*

Using the principle of balancing the momentum flux from the stellar wind and motion of the ambient ISM, a relation stellar wind parameters and ambient ISM characteristics can be shown as,

$$\rho_w V_w^2 = \rho_a V_a^2 \ . \tag{1}$$

In Equation 1, ρ_w is the density of the stellar-wind, V_w is the speed of the stellar-wind, ρ_a is the density of the surrounding interstellar medium, and V_a is the speed of the bulk motion of the ambient ISM in the star's rest frame. Assuming an isotropic wind, the stellar wind-density can be written as

$$\rho_w = \frac{\dot{M}}{4\pi R_0^2 V_w} \ , \tag{2}$$

where R_0 is the distance from the central star to the shock front. Inserting the result of Equation 2 into Equation 1 and solving for $\dot{M}$ results in

$$\dot{M} = \frac{4\pi R_0^2 V_a^2 \rho_a}{V_w} \ . \tag{3}$$

The quantity R_0, can be rewritten as the angular standoff distance, R_{0r}, as measured from IR data, times the parallactic distance, D. Equation 3 can then be rewritten as

$$\dot{M} = \frac{4\pi R_{0r}^2 D^2 V_a^2 \rho_a}{V_w} \ . \tag{4}$$

To measure the ambient density of the ISM, ρ_a, the mass density of the ISM can expressed as

$$\rho_a = n_a \overline{m} \ , \tag{5}$$

where n_a is the ambient number density of the local environment and $\overline{m}$ is the mean particle mass ($\overline{m} = 2.3 \times 10^{24}$ g, for the standard value used for the Milky Way ISM). The ambient number density, n_a, can be challenging to measure. The number density along the shock front, n_N, is easier to obtain since the shock front is luminous at IR wavelengths due to warm dust emission. Since n_a should scale linearly with n_N, the latter can be used as a proxy for the former. The number density along the shock front can be given as

$$n_N = \frac{I_\nu}{\ell j_\nu} \ , \tag{6}$$

in which I_ν is the specific intensity measured at the shock front at either 24 or 70 μm in units of Jy sr^{-1}, ℓ is the chord length, the distances across the bowshock, and j_ν is the dust emissivity in Jy cm^2 sr^{-1} nucleon^{-1}. The relation in Equation 6 assumes that the emission across the shock-front is isotropic through the chord length ℓ. The dust emissivity j_ν is calculated from Draine & Li (2007) Milky Way dust models. Draine & Li (2007) tabulated dust-emissivity j_ν as a function of wavelength and as a function of the normalized ionization parameter, U, under different PAH concentrations. The Draine & Li (2007) ionization parameter U is defined as

$$U = \frac{R_*^2 \sigma T_{\rm eff}^4 / \left(R_0^2 c\right)}{u_{\rm MMP83}} \ , \tag{7}$$

with σ and c having their traditional meanings and $u_{\rm MMP83}$ being the mean interstellar radiation field (ISRF) for the Milky Way in units of erg s^{-1} cm^{-2} c^{-1} determined by Mathis et al. (1983).

In this work, I interpolate between the tabulated values for j_ν as a function of $\log U$ (Draine & Li 2007), and use this to calculate a j_ν for each star. I assume minimal PAH concentration of 0.47%, as PAHs are likely destroyed in the region of the shock-front. I strive to use j_ν for 70 μm however in the case where there is no detectable bowshock in 70 μm, use 24 μm data.

With I_ν and ℓ measured from either 24 μm or 70 μm data, and j_ν interpolated from Draine & Li (2007) models, the number density along the shock-front, n_N, can be obtained using equation 6. Figure 7 plots j_ν as a function of the ionization parameter U in both the 24 and 70 μm cases from models presented in Draine & Li (2007). The lowest PAH concentration is assumed as PAHs are likely destroyed in the environment near the shock front. With an estimate of the number density

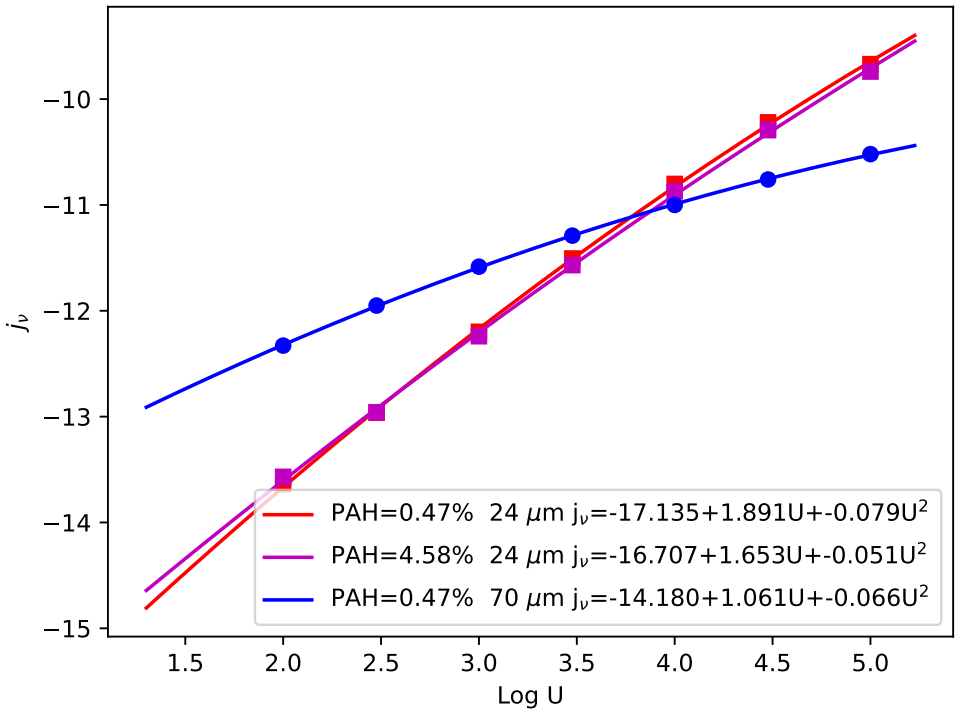

Figure 7. Interpolation of j_ν values as a function of $\log U$ as tabulated by Draine & Li (2007), with quadratic fits displayed in the legend for each data set. PAH concentrations of 0.47% were used in both 24 μm and 70 μm cases. A PAH concentration of 4.58% fit is shown in 24 μm is shown for comparison.

along the shock-front, the ambient number density, n_a, becomes obtainable. As mentioned before, I expect n_N to scale linearly with n_a. A typical assumption is that density increases by a factor of four across a shock (Landau & Lifshitz 1987), thus yielding the relation

$$n_a = 0.25 n_N \ . \tag{8}$$

Combining the results of Equations 5, 6 and 8 into Equation 4 yields

$$\dot{M} = \frac{\pi R_{0r}^2 D^2 V_a^2 \overline{m} I_\nu}{\ell j_\nu V_w} \ , \tag{9}$$

The relation between ℓ, the linear chord distance of the bowshock, ℓ_r, the angular chord distance of the bowshock is

$$\ell = \ell_r D \ . \tag{10}$$

Equation 10 can be substitute into Equation 9 yielding

$$\dot{M} = \frac{\pi R_{0r}^2 D^2 V_a^2 \overline{m} I_\nu}{\ell_r D j_\nu V_w} \ . \tag{11}$$

This equation can further be reduced by canceling distance D from the numerator and denominator yielding

$$\dot{M} = \frac{\pi R_{0r}^2 D V_a^2 \overline{m} I_\nu}{\ell_r j_\nu V_w} \ . \tag{12}$$

Equation 12 can be rewritten in terms of convenient units as

$$\dot{M}\left(M_\odot \text{ yr}^{-1}\right) = 1.67{\times}10^{-28}{\times}\frac{\left[R_0\,(\text{arcsec})\right]^2 D\,(\text{kpc})\left[V_a\,(\text{km s}^{-1})\right]^2 I_\nu\,(\text{Jy sr}^{-1})}{V_w\,(\text{km s}^{-1})\,\ell\,(\text{arcsec})\,j_\nu\,(\text{Jy cm}^2\text{ sr}^{-1}\text{ nucleon}^{-1})} \text{ (Kobulnicky et al. 2018).} \tag{13}$$

Parameters R_0, I_ν, and ℓ are directly measurable using *SST* images described in Section 1.4. D and V_a are obtained by using Gaia DR3 archival parallax and proper motion data. V_w is characteristic of the star's spectral type (measured from blue optical spectra) and obtained from tabulated values in Mokiem et al. (2007).

1.4.3. *Stellar parameters from optical spectra*

The problem of quantitative analysis from stellar spectra can be harder than it seems. Those unacquainted with the task are familiar with the idea of obtaining information from spectra but the actual process of doing so can be intricate, and several independent methods of extracting information from stellar spectra have been developed (Simón-Díaz 2020). The three primary techniques that have been developed are line ratio comparisons, cross-correlations, and pixel-pixel χ^2 analysis. Each method has its strengths and limitations. I will use the latter of these techniques and minimize the χ^2 between an observed spectrum and a grid of stellar model atmosphere spectra, interpolating the models where necessary over the fundamental stellar parameters temperature, surface gravity, and projected rotational velocity[1]. The benefits of this method is this technique utilizes all available lines to constrain retrieved stellar parameters. Individual lines can be degenerate to changes in gravity and $T_{\rm eff}$, so the analysis of only a few lines can be ambiguous in certain regimes. The drawback of this method is that it requires a robust grid of model spectra to interpolate over.

As a pilot study, I obtained 64 optical spectra of central stars powering bowshock nebulae were obtained from Wyoming Infrared Observatory 2.3 m telescope (WIRO) long-slit spectrograph and Apache Point Observatory Kitt Peak Ohio State Multi-Object Spectrograph ((KOSMOS) Martini et al. 2011). At WIRO the spectrograph is 600 l mm^{-1} grating with the 1.2" slit in second order to obtain spectra over the wavelength range $\lambda\lambda$4000–5000. This configuration yielded a dispersion of 1.10 Å pixel^{-1} with a resolution of $R = 1,500$. At APO the KOSMOS spectrograph is uses a 704 l mm^{-1} blue grism with the 0.83" low slit in second order to obtain spectra over the wavelength range $\lambda\lambda$3700–6200 Å. This configuration yielded a dispersion of 0.68 Å pixel^{-1} with a resolution of $R = 2,500$. The gratings for both spectrographs were chosen as many of the characteristic transitions in OB spectra occur in the range $\lambda\lambda$4000–5000 Å (Gray & Corbally 2009). Exposure times of 2x45 seconds and 2x1200 seconds for $B_P = 8.7 - 14.3$ targets yielded spectra with signal to noise ratios of 90:1 and 30:1 pixel^{-1} at 4200 Å respectively. Figure 8 presents a continuum-normalized optical spectrum of ζ Oph (central star of bowshock nebulae 013 from the catalogue of Kobulnicky et al. (2017), hereafter referred to as BS013*) with temperature- and gravity-sensitive lines labeled. The Figure includes regions of the spectrum containing most of the important diagnostic spectral features.

[1] Given that my targets are young stars within four kiloparsecs of the Sun in the plane of the galaxy, I assume Solar metallicity (see Figure 3 of Kobulnicky et al. 2019).

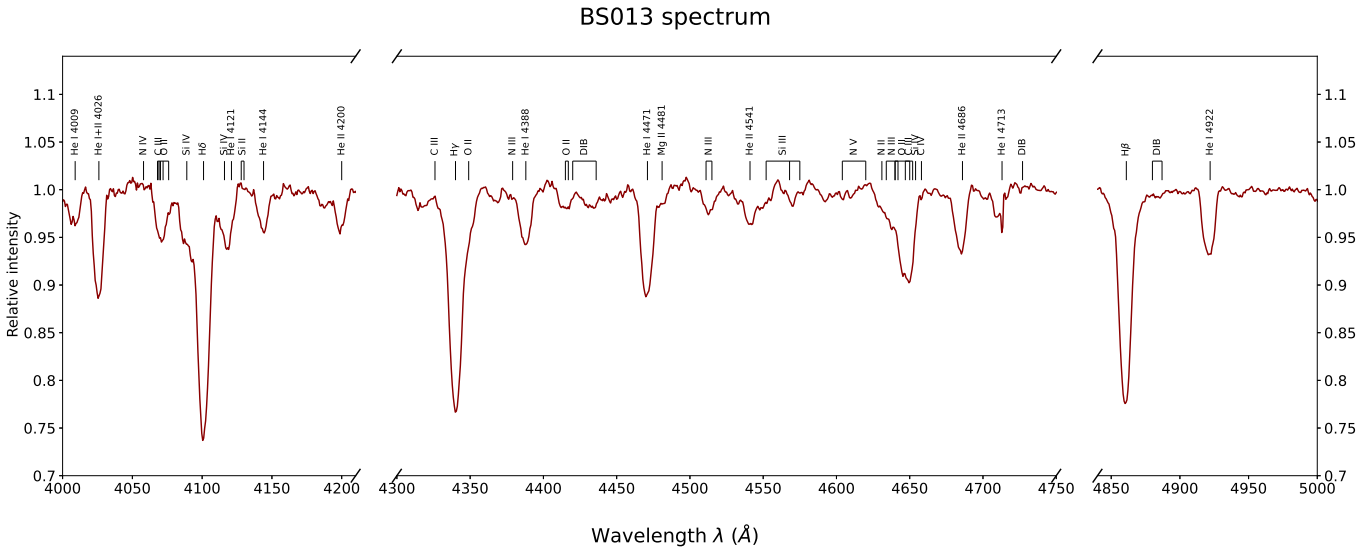

Figure 8. APO spectrum of ζ Oph. Characteristic transition lines are labeled. The ranges $\lambda\lambda$4200–4300 Å and $\lambda\lambda$4750–4850 Å are hidden because of the lack spectral features in this range for OB stars.

The presence of He I and He II identify this star as a hot star. The ratio of the He II to He I lines is an important temperature diagnostic. Additionally, the ratio of Si IV to Si III also serves as a temperature diagnostic in this range.

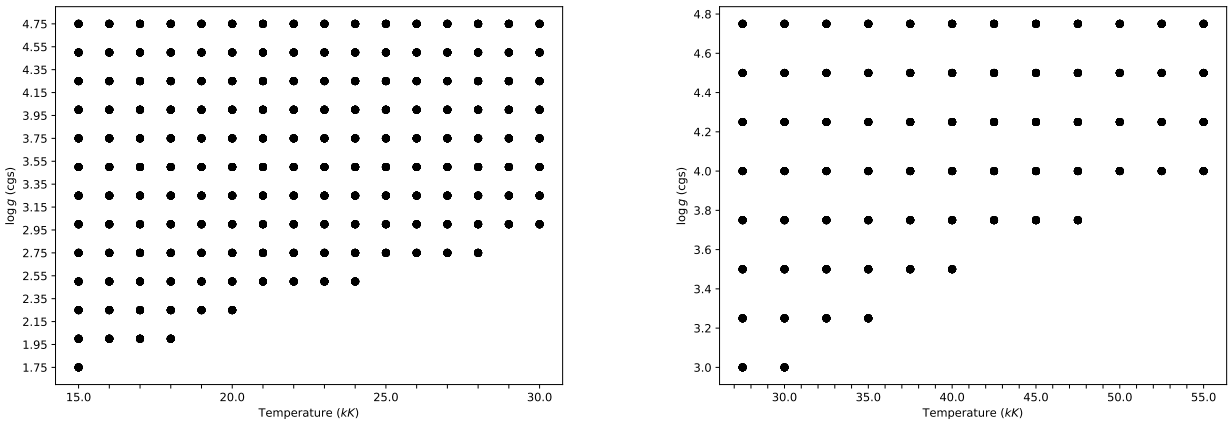

Figure 9. TLUSTY BSTAR 2006 and OSTAR 2002 model grids.

I used the TLUSTY OSTAR2002 (Lanz & Hubeny 2003) and BSTAR2006 (Lanz & Hubeny 2007) grids of models to determine fundamental stellar parameters for my targets. The TLUSTY OSTAR2002 models are a grid of metal line-blanketed NLTE model atmospheres spanning $T_{\rm eff}$ from 27,500 K through 55,000 K in steps of 2,500 K, and $\log g$ from 3.0 to 4.75 in steps of 0.25 dex. Similarly, the TLUSTY BSTAR2006 models are a grid for temperatures $T_{\rm eff}$ ranging from 15,000 K to 30,000 K in steps of 1,000 K and $\log g$ as low as 1.75 dex to 4.75 in steps of 0.25 dex. Figure 9 shows the available parameters for both model libraries. These grids cover the expected temperature and gravity range of my targets.

In the first step of the stellar spectral analysis, my code[2] determines the best-fit model spectrum amongst the OSTAR and BSTAR grids. I rotationally broaden all model spectra to the resolution of the KOSMOS or WIRO longslit spectrographs with additional rotational broadenings ranging from 50 to 500 km s^{-1} in steps of 50 km s^{-1} using the `rotin` convolution program. I then re-interpolate the model spectra at the wavelengths of the data. My code determines the best-fit model by calculating the absolute pixel-pixel deviations between all the models and the stellar spectrum in the $\lambda\lambda$4000–5000 Å range and chooses the model with the smallest summed deviation. Once the best-fit model is determined, the model library is restricted to either the TLUSTY OSTAR or TLUSTY BSTAR grids, depending on which library the best-fit model belongs to. Restricting the fitting program to work within one of the sets of models prevents complications of interpolating between the parameter space where the two sets of models overlap, the temperature range $T_{\rm eff} = 27,500$–$30,000$ K.

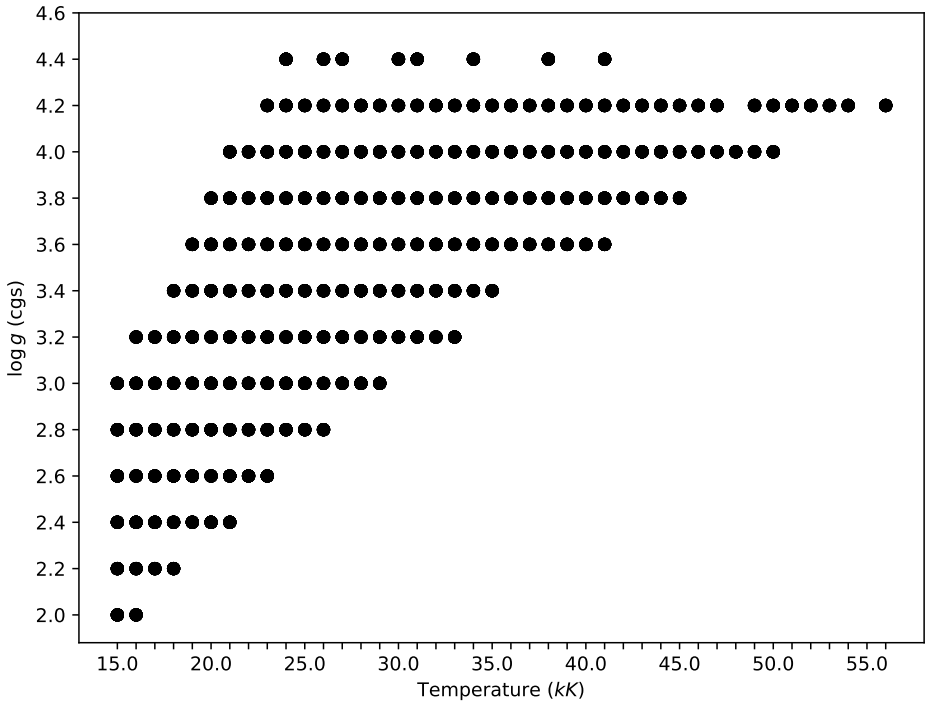

Figure 10. Parameter space spanned by the PoWR grid of models. The PoWR models cover a smaller range of $T_{\rm eff}$ and $\log g$ than the TLUSTY models, most notably lacking high-surface-gravity B-dwarfs (upper left) and O giants/super-giants (lower right), despite finer gridding.

I considered using the Potsdam Wolf-Rayet (PoWR) grid of models (Hainich et al. 2019). The PoWR models are an improved library of model OB atmospheres, calculated with the PoWR code, designed to calculate model spectra for massive stars with expanding atmospheres and accounts for NLTE effects, line-blanketing, and wind inhomogeneities. More sophisticated models should provide better fits of the spectra of hot stars. Some spectral lines, mostly C/N/O features in giant/supergiant

[2] The spectral fitting routine I developed is available on my Github: https://github.com/n-patten/Bowshocks/blob/main/temp.py

spectra, that did not provide good fits to the TLUSTY models showed better agreement with the PoWR models. Nevertheless, I found that the best fitting temperatures and gravities were very close to those found with TLUSTY models. Therefore, I decided to use the TLUSTY models because the they covered a wider range of temperatures and gravities. 10 presents the parameter space spanned by the PoWR grid of models. Although these models provide superior fits ($\chi^2_{\rm red}$ =1.26 vs 1.33 for B1Ia BS361*) with finer gridding in temperature and gravity, the parameter space spanned by the PoWR models is insufficient to capture the entire range spanned by stars central to bowshock nebulae.

After determining a best-fit model and model library to work within, I calculated the uncertainty spectrum using a procedure inspired by the works of Irrgang et al. (2014) and Czekala et al. (2015). The uncertainty at each pixel can be thought to have two components: a statistical component, $\sigma_{\rm stat}$, that is dependent on the signal-to-noise ratio of the spectrum itself, and a systematic component, $\sigma_{\rm sys}$, representing fundamental differences between the models and stellar spectrum. These uncertainties should add in-quadrature. This relation can be expressed by,

$$\sigma^2_{\rm total} = \sigma^2_{\rm stat} + \sigma^2_{\rm sys} \ . \tag{14}$$

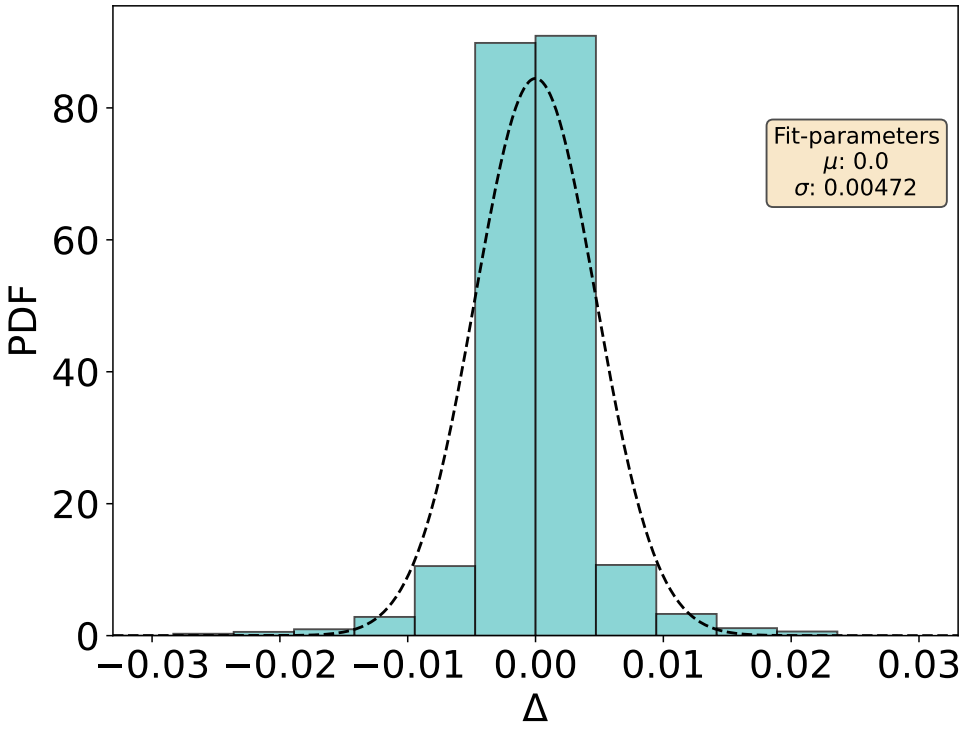

Figure 11. Noise distribution for Bowshock object BS013*. A normal-distribution is fitted and overplotted with the best-fit parameters in the text box.

The statistical uncertainty is calculated by measuring the dispersion between two neighboring pixels separated by a one-pixel gap; this accounts for the correlation between adjacent pixels in the spectrum. Represented mathematically, the dispersion for the $i^{\rm th}$ pixel can be expressed as the quantity Δ_i defined as

$$\Delta_i = n_i - \frac{1}{2}\left(n_{i-2} + n_{i+2}\right) \ , \tag{15}$$

with n_i, n_{i-2}, and n_{i+2} representing the normalized flux value at pixels i, $i-2$, and $i+2$ respectively.

Figure 11 shows a histogram of neighboring pixel deviations, Δ_i, for BS013*. The dashed line is the best-fit Gaussian to the distribution to the distribution of deviations Δ_i. The dispersion of the Δ_i is approximately a Gaussian as expected. The width of this distribution is $\sigma = 0.005$, representing the statistical component of the uncertainty for each pixel $\sigma_{\rm stat}$ in this signal-to-noise ratio 200:1 spectrum, measured empirically at 4500 Å.

To estimate $\sigma_{\rm sys}$, a different approach must be used. First, it is important to note that the systematic uncertainty represents fundamental differences between the suite of model spectra and the data, and as such, will be a wavelength array of quantities rather than a single value. This is difficult to quantify from first principles as this requires prior information as to which spectral features will differ between the model and data. There are several reasons why a spectrum may differ from a model spectrum. Data may include interstellar features not included in a model. Spectra of real stars may reflect physical phenomena not included or imperfectly characterized by the model. Model spectra necessarily include assumptions about mixing, microturbulence, rotation, abundances, and cannot be expected to perfectly recreate real spectra. The result of these assumptions creates mismatches between spectra and models, most dramatically in spectral features. Given the expectation of systematic differences between data and models, I define

$$\sigma^2_{{\rm sys},i} = \begin{cases} R_i^2 - \sigma^2_{\rm stat} & \text{if } |R_i| > |\sigma_{\rm stat}| \\ 0 & \text{if } |\sigma_{\rm stat}| > |R_i| \end{cases} \ , \tag{16}$$

where R_i represents the difference between the best-fit model from the stellar spectrum at the $i^{\rm th}$ pixel. The systematic uncertainty spectrum exceeding $\sigma_{\rm stat}$ is then smoothed by three resolution elements to obtain a characteristic σ that is smaller than the full envelope of deviations from the model.

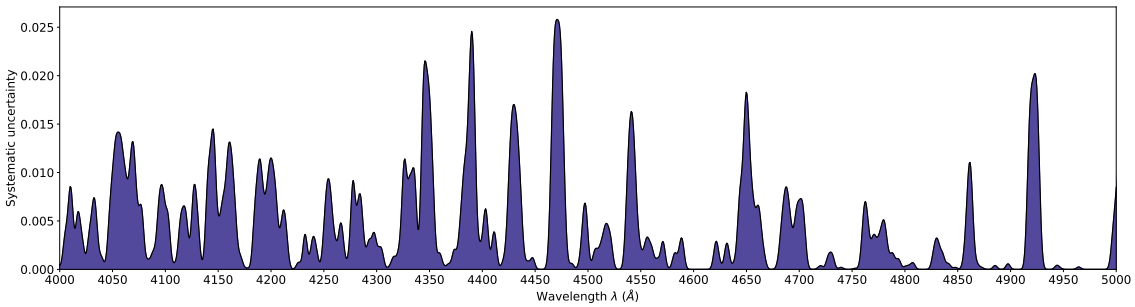

Figure 12. The systematic uncertainty, $\sigma_{\rm sys}$, at each wavelength for BS013*.

Figure 12 displays the $\sigma_{\rm sys}$ spectrum, calculated for BS013*. The $\sigma_{\rm sys}$ equals zero where $\sigma_{\rm stat}$ is sufficient to encompass the total uncertainty. The $\sigma_{\rm sys}$ spectrum contains peaks at the location of spectral features, most notably at the Balmer series and He I and He II lines. This demonstrates that many of the absorption lines are not well fit in any model, regardless of the model broadening.

Broad low-amplitude peaks in the $\sigma_{\rm sys}$ spectrum, for example at λ4430 and λ4865, are the signatures of diffuse interstellar absorption bands. The horizontal line at $\sigma \approx 0.004$ designates the statistical uncertainty. Over most of the wavelength range, the majority of the uncertainty is dominated by systematic disagreement with the model. The spectrum of BS013* is a high signal-to-noise ratio spectrum, and so it would intuitively make sense that most of the error budget is due to systematic deviations from the model. In spectra with lower signal-to-noise ratios and larger statistical uncertainties, the statistical component of the uncertainty will dominate.

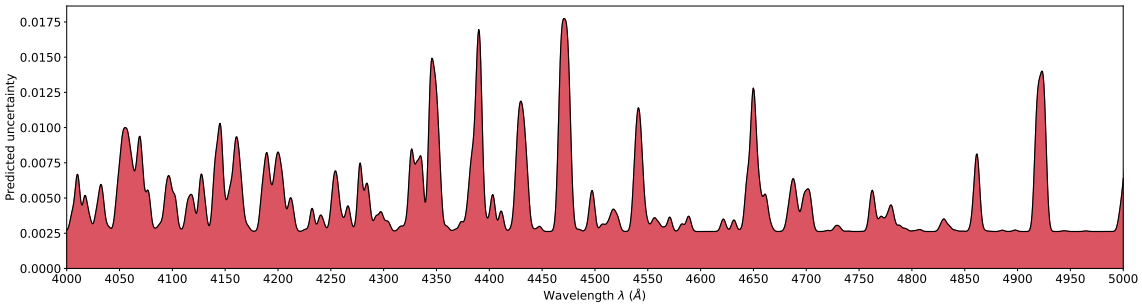

Figure 13. Total uncertainty, $\sigma_{\rm tot}$ as function of wavelength for BS013*.

With an estimate on $\sigma_{\rm tot}$ and $\sigma_{\rm sys}$, I use Equation 14 to estimate the total uncertainty at each pixel. Figure 13 shows the result of this analysis and plots the total uncertainty, $\sigma_{\rm tot}$, as a function of wavelength. The regions where $\sigma_{\rm sys}$ was 0 in Figure 12, have now been replaced by the estimate of $\sigma_{\rm stat}$ from Figure 11.

I used a trilinear interpolation over the grid of temperatures, gravities, and rotational velocities to produce models with a continuous range of each parameter to compare with the data. Using an MCMC (Foreman-Mackey et al. 2013) sampler, my program explores the available parameter space, with flat priors, to find the best-fitting set of stellar parameters to match the data. I use the $50^{\rm th}$ percentile as the median value. My program characterizes the 1σ uncertainties in the stellar parameters by selecting the $16^{\rm th}$ and $84^{\rm th}$ percentiles from the posterior distributions.

Figure 14 shows the spectrum of BS013* over-plotted with the best-fit interpolated model in the top panel with the residual spectrum and the 1, 2, and 3 σ uncertainties (shown by three different opacity envelopes) in the bottom panel. Important temperature- and gravity-sensitive lines are labeled, as well as diffuse interstellar absorption bands (DIBs). Gravity-sensitive lines, such as Si, C, N, and O are well-fit by the model. Temperature-sensitive lines, such as H, He I, and He II are also well-fit, but the depth of these lines does not perfectly agree with the model; it is here that the residuals in the lower panel are the largest. The lines of ionized He, Si, C, N, and O are also in agreement with the models. The widths of the rotationally broadened models show good agreement with the data indicating that an optimal broadening has been used.

Figure 15 shows the posterior distribution of the fitted stellar parameters. The widths of these distributions quantify the uncertainty on each parameter. For BS013*, we retrieve a temperature of 32240^{+527}_{-384} K, $\log g$ of $3.71^{+0.07}_{-0.05}$ dex, and a $v \sin i$ of $361^{+12.59}_{-11.53}$ km s^{-1}. Temperature and surface gravity compare favorably with other published values for BS013*. Holgado et al. (2022) find a $T_{\rm eff} = 32000 \pm 500$ K and $\log g = 3.75 \pm 0.05$. Repolust et al. (2004) find similar values with a

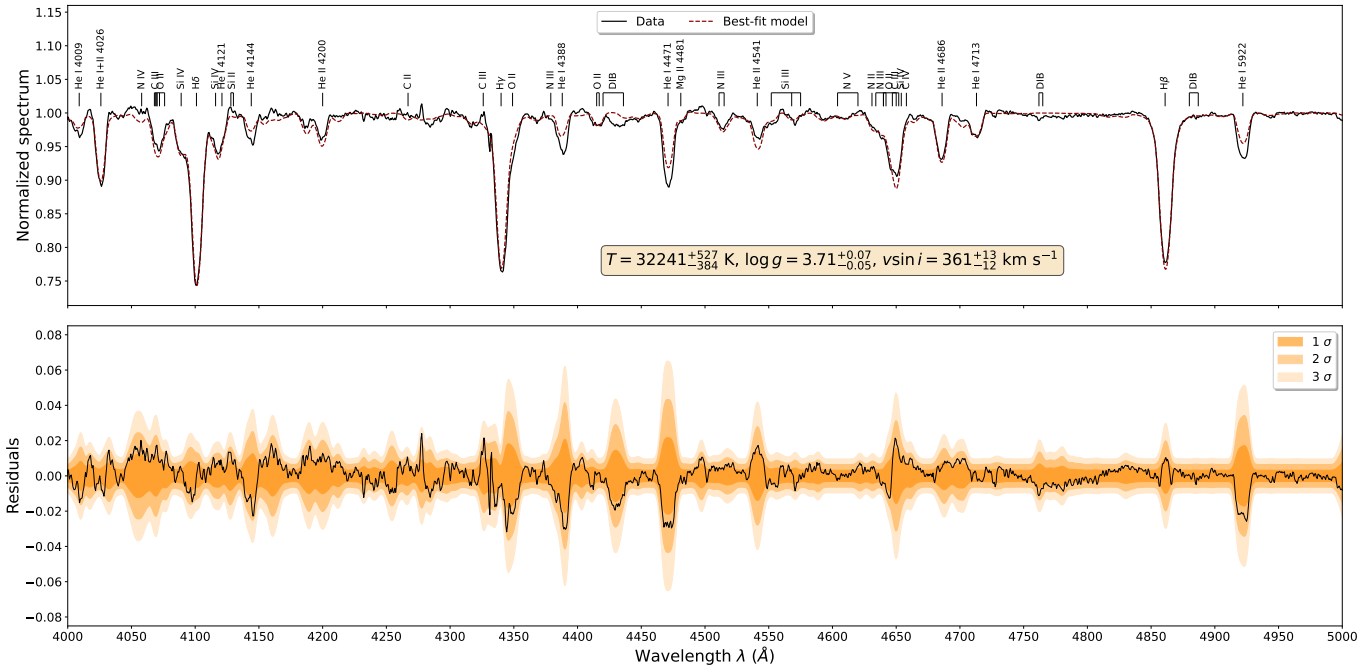

Figure 14. Top: Normalized stellar spectrum (black) with best-fit interpolated model spectrum (dashed red) overplotted. Absorption features sensitive to changes in $T_{\rm eff}$ and $\log g$ are labeled. The best-fit stellar parameters are presented in the beige box in the bottom of the plot. Bottom: Residual spectrum (black) with shaded regions indicating the one, two and three-sigma uncertainties at each pixel.

$T_{\rm eff} = 32000$ and $\log g = 3.85$. Literature values for $v \sin i$ range between 328 and 385 km s^{-1} (Holgado et al. 2022; Simón-Díaz & Herrero 2014).

My approach of considering statistical and systematic uncertainties on a pixel-pixel basis allows me to achieve tighter constraints on stellar parameters than would be possible with statistical Poisson-noise alone. Pixels that are associated with spectral features that are discordant with the set of models have a greater uncertainty to prevent them from dominating the χ^2. This allows for an emphasis on the temperature- and gravity-determining features in the fitting process. By characterizing features that fundamentally differ from the models, and accordingly inflating the uncertainty in these regions, we are better able to determine the uncertainties of the fitted stellar parameters. The sensitivity of this line-based analysis is reflected in the uncertainties of the outputted stellar parameters. When only considering statistical noise, the uncertainty in the temperature was on the order of 10^3 K and the uncertainty in $\log g$ was approximately 0.3 dex. My revised analysis can be expected to yield uncertainties of a few hundred Kelvin in temperature and ≤ 0.1 dex in $\log g$.

To verify my analysis technique, I observed a set of 15 stars with $T_{\rm eff}$, $\log g$, and $v \sin i$ measured in the literature to compare my retrieved values with published results. Table 1 lists the 15 stars used in this calibration sample. The first column lists the Henry Draper catalogue identification number of each calibration star, the second and third columns list the literature and this work's values for $T_{\rm eff}$ in units of Kelvin, the fourth and fifth columns list the literature and this work's values for surface-gravity in cgs units, the sixth and seventh columns list the literature and this work's values for the

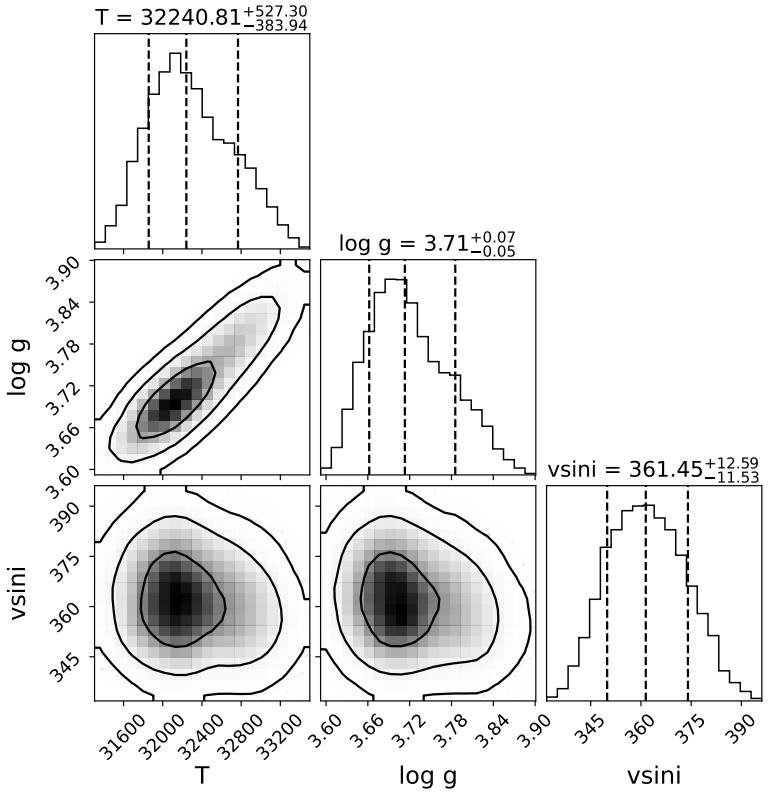

Figure 15. Posterior distribution of fitted parameters for BS013*.

projected rotational-velocity in km s^{-1}, and the eighth column lists the reference(s) used to obtain literature values. Some stars required the citation of two works for all three parameters. In this case, the first citation indicates the reference for temperature and gravity information, and the second citation is the reference for rotation. Numbers in parentheses next to values indicate uncertainties in each respective parameter. If no literature uncertainty is reported, an error of 500 K, 0.05 dex, and 10% in $v \sin i$ is adopted.

Figure 16 (left panel) compares the literature temperatures to my retrieved values. Each point represents a calibration star, with vertical and horizontal error bars corresponding to respective uncertainties in each measurement. The black dashed line is the one-to-one comparison line. There is excellent agreement between my results and literature values. The right panel plots a horizontal histogram for temperatures from bowshock stars in my pilot study. Most of the studied stars lie in the temperature range of my calibration sample. Only four stars are slightly hotter than the hottest star in my calibration sample, but a small extrapolation of the one-to-one is reasonable.

Figure 17 (left panel) plots retrieved values of $\log g$ versus literature values for the calibration sample, similar to Figure 16. As in Figure 16, the right panel is a horizontal histogram of bowshock stars in my pilot study. Most of the studied bowshock stars lie within the confirmed region of agreement, however a few stars in the pilot study have a $\log g$ slightly greater than 4.5. The nature of these high-$\log g$ stars will be examined in the course of this study. Since agreement has been demonstrated in the calibration sample, it is reasonable to assume this agreement extends for slightly higher $\log g$.

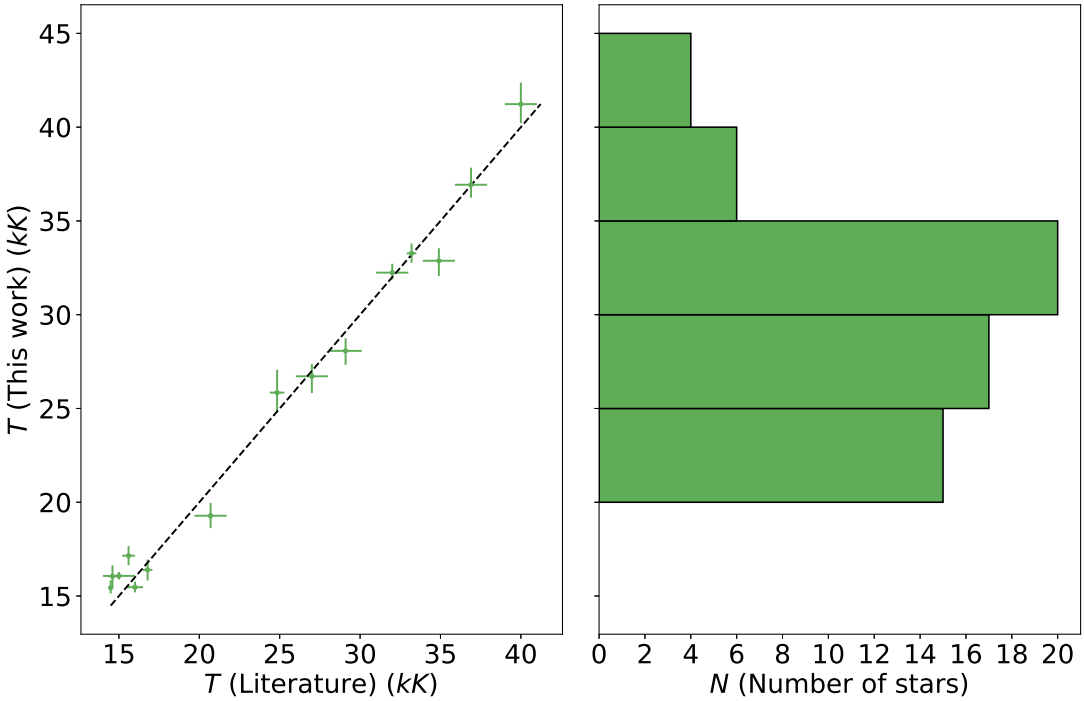

Figure 16. Left: Retrieved temperatures versus literature values for the calibration sample listed in Table 1. Right: A histogram plotting the temperatures of the bowshock stars in the pilot study.

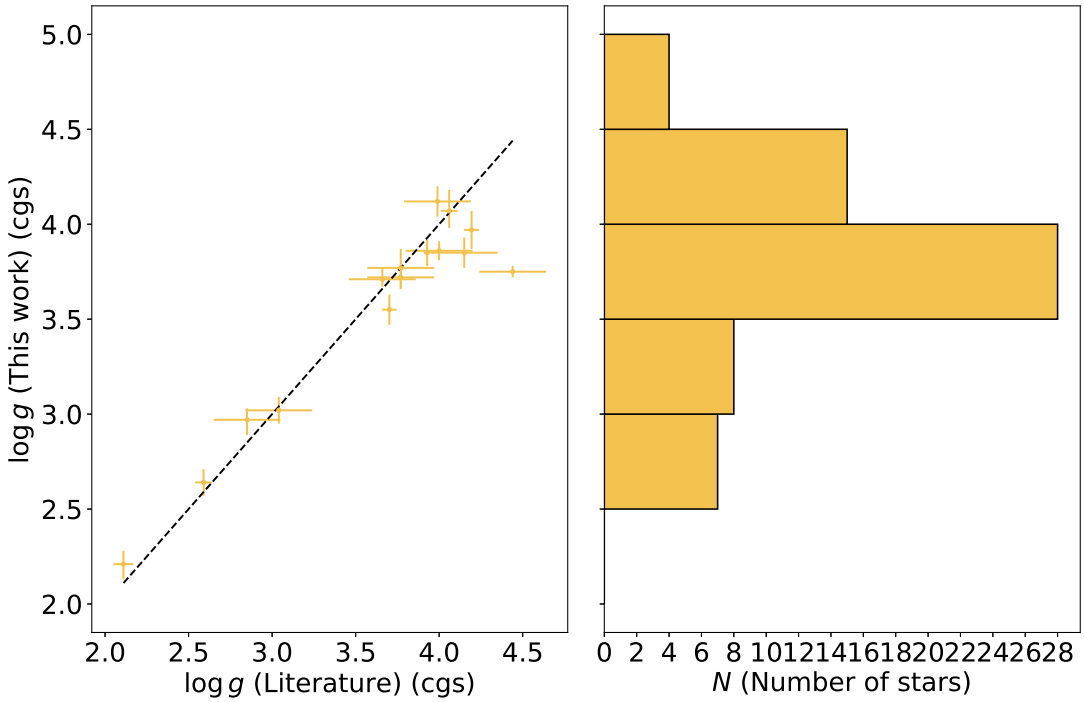

Figure 17. Left: Retrieved $\log g$ versus literature values for the calibrations sample, as in Figure 16. The black dashed line is the one-to-one comparison. Right: A histogram plotting the $\log g$ of the bowshock stars in the pilot study.

Table 1.

	$T_{\rm eff}$ (K)		$\log g$ (dex)		$v \sin i$ (km s^{-1})		
HD	literature	this work	literature	this work	literature	this work	Reference(s)
24431	34900	32877 (740)	3.77	3.77 (0.11)	49	97 (22)	1
29309	16785 (300)	16395 (560)	3.702 (0.043)	3.55 (0.08)	38 (12)	41 (30)	2
30870	14490 (150)	15443 (350)	3.928 (0.021)	3.85 (0.07)	91 (8)	56 (45)	2
34078	33200 (200)	33272 (520)	4.06 (0.05)	4.07 (0.10)	9 (2)	36 (22)	3
34989	24838 (450)	25847 (1130)	4.194 (0.44)	3.97 (0.10)	30 (16)	27 (19)	2
36013	15000	16073 (200)	4.44	3.75 (0.03)	182	259 (16)	4
36371	14600 (300)	16055 (570)	2.11 (0.06)	2.21 (0.08)	36 (5)	33 (22)	5
36879	36900	36929 (800)	3.77	3.72 (0.06)	209	199 (18)	1
37128	27000	26716 (775)	2.85	2.97 (0.07)	55	32 (21)	6, 7
42088	40000	41228 (1083)	3.99	4.12 (0.08)	49	55 (31)	1
45418	16000 (500)	15471 (286)	4.00 (0.20)	3.86 (0.05)	229 (15)	197 (21)	8, 9
47432	29100	28072 (710)	3.94	3.02 (0.07)	97	48 (34)	1
51309	15600 (400)	17150 (510)	2.59 (0.05)	2.64 (0.07)	30 (6)	26 (18)	5
61347	...	32537 (570)	...	3.46 (0.06)	112	95 (38)	10
149757	32000	32242 (422)	3.66	3.71 (0.05)	385	361 (12)	1

NOTE—References: (1) Holgado et al. (2022); (2) Huang et al. (2010); (3) Aschenbrenner et al. (2023); (4) Kounkel et al. (2019); (5) Weßmayer et al. (2022); (6) Crowther et al. (2006); (7) Burssens et al. (2020); (8) Mugnes & Robert (2015); (9) Bragança et al. (2012); (10) Simón-Díaz et al. (2017).
Literature and measured values for stellar parameters for bright OB stars used to compare spectral-fitting routine. Numbers in parentheses are the associated uncertainty. The last column is the references used for literature values. In the case where two references are listed, the first reference was used for $T_{\rm eff}$ and $\log g$ and the second references was used for $v \sin i$.

Figure 18 (left panel) compares retrieved and literature $v \sin i$ for the calibration sample. The plot shows a strong correlation. However, this correlation is driven by the four data points above $v \sin i$ of 100 km s^{-1}. Below this value, the data show no correlation. This results from the fact that KOSMOS is a low-resolution spectrograph ($R \sim 2500$) and is not specifically intended for rotational-broadening studies. It has an instrumental resolution of ≈120 km s^{-1}, which imposes a floor, below which rotational broadenings cannot be measured. Additional calibration stars would help determine the velocity threshold where rotational broadening becomes measurable. The right panel is a histogram of the rotational velocities in the pilot study. Almost all bowshock objects lie within the calibrated regime. More problematic, however, is that a large fraction of bowshock stars fall below the 100 km s^{-1} resolution limit. As shown in the histogram in Figure 17, a significant portion of bowshock stars in the pilot study fall in the giant ($\log g \sim 3.5$) or the super-giant ($\log g \sim 3.0$) regimes. As a rapidly-rotating star evolves and expands, its rotational velocity will decrease to conserve angular momentum. This explains why a significant fraction of bowshock stars show small

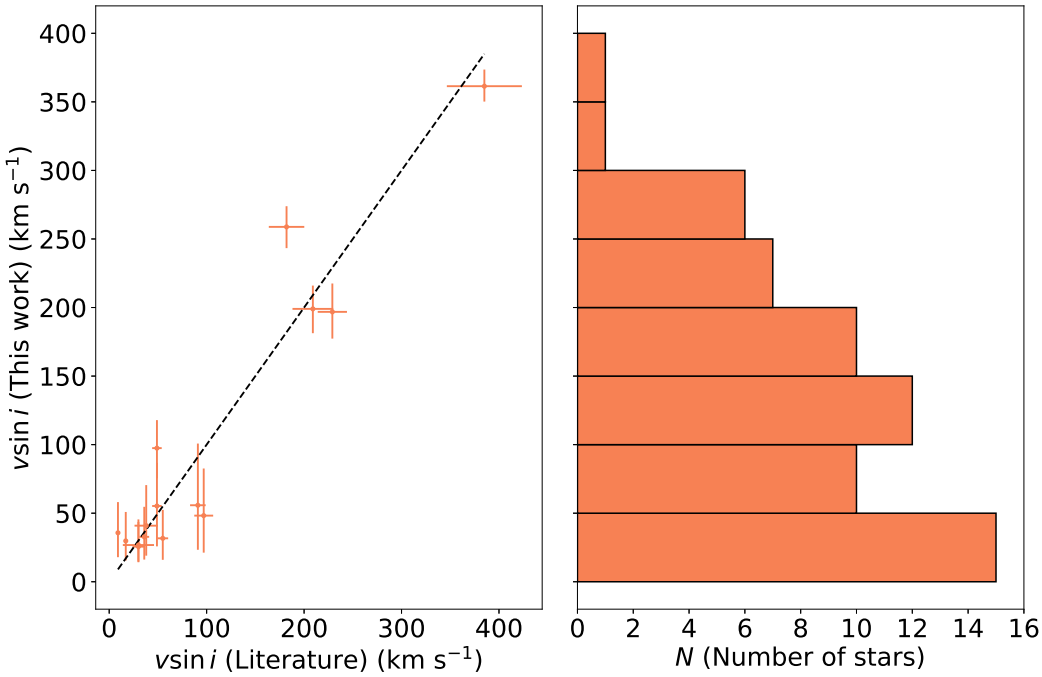

Figure 18. Left: Retrieved $v \sin i$ versus literature values for the calibration sample, as in Figure 16. Right: A histogram plotting the $v \sin i$ of the bowshock stars in the pilot study.

rotational velocities. Rotational velocity does not play an explicit role in calculating mass-loss, but I may consider it a tertiary parameter of interest if suitable data are available.

1.5. *Dissertation Questions*

1.5.1. *Question I: How does mass loss change as a function of stellar parameters?*

I hope to provide new measurements of mass loss as a function of stellar parameters temperature $T_{\rm eff}$, surface gravity $\log g$, and possibly rotational velocity $v \sin i$. I will compare my new results with other canonical techniques and theoretical predictions to help mass-loss rates for approximately 120 massive stars, drawing from the Kobulnicky et al. (2016) bowshock sample. I will obtain optical-blue spectra to better-determine stellar parameters $T_{\rm eff}$ and $\log g$ than was previously done in Kobulnicky et al. (2019), which was limited to classification from optical-red spectra. In my pilot study, I have obtained ≈60 spectra with adequate signal-to-noise-ratio to characterize the fundamental stellar parameters. I hope to double this number over the next year. I will use *SST* images to measure the standoff distances, and chord lengths as was done in previous works. I will use improved Gaia DR3 astrometry to obtain space velocities for my bowshock stars, which Kobulnicky et al. (2019) did not have access to. Figure 19 plots preliminary results from analysis in my pilot study. The dots represent a measurement in my pilot study, colored by their respective surface-gravities. Each measurement of mass loss is connected by the dashed vertical line to its respective Vink et al. (2001) prediction. Colored red and magenta track represent theoretical predictions from Lucy (2010) and Krtička (2014) respectively. My eventual thesis sample will triple the sample size to better address how mass-loss rate changes with fundamental stellar parameters.

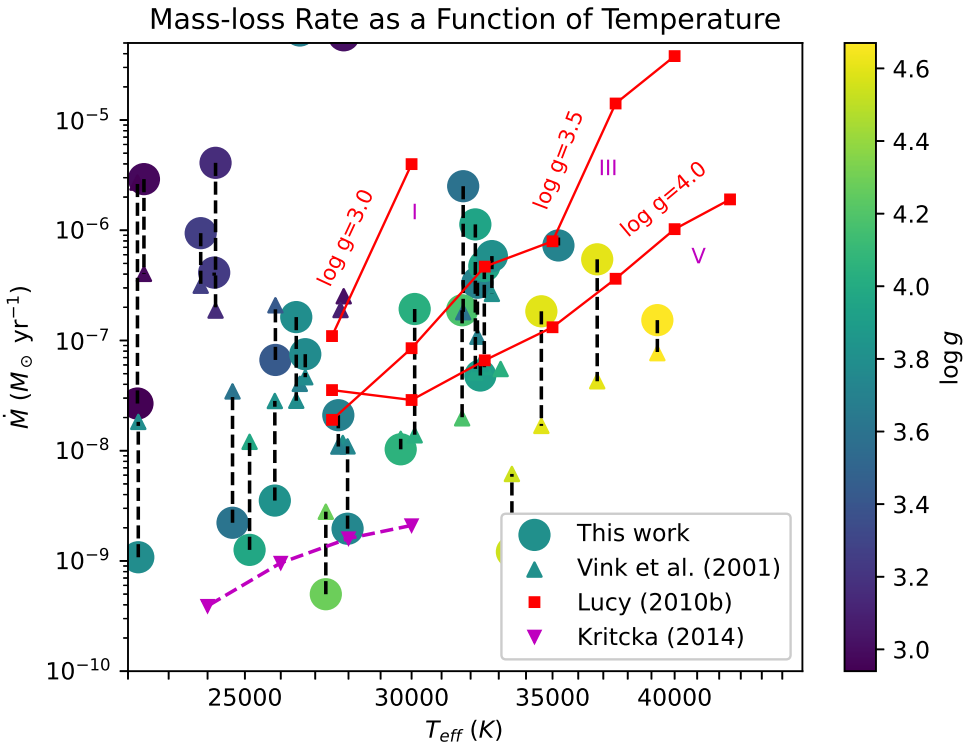

Figure 19. Mass-loss as a function of $T_{\rm eff}$ and $\log g$ for 40 stars in my pilot study.

Table 2.

Bowshock Parameter(s)	Source	Observed	Goal
(1)	(2)	(3)	(4)
$T_{\rm eff}$,$\log g$,$v \sin i$	Blue Spectra	64	120
R_0,ℓ,I_ν	*SST*	40	120
D,V_a	Gaia Astrometry	∼120	120
V_w	Blue Spectra, literature	40	120

NOTE—Bowshock parameters needed to calculate mass loss grouped by source.

Table 2 lists the number of obtained parameters in my pilot study and my overall goal. Column (1) gives the each bowshock parameter, grouped by how it is obtained. Column (2) lists the source of the parameter in Column (1). Column(3) lists how many central bowshock stars have already been measured in my pilot study. Column (4) lists what my dissertation goal is. In determining I_ν and j_ν, 70 μm data is preferred to avoid stochastic heating effects thought to be present in 24 μm data

(Kobulnicky et al. 2019). Some bowshock nebulae however, show no detections above background levels in 70 μm images. This may necessitate using 24 μm images, bearing in mind systematic errors that may arise with the use of these data. Currently, I have measurements for 26 bowshocks in 24 μm and 19 bowshocks in 70 μm. The limiting factor in how many bowshock stars I can study is how many blue spectra I can obtain since the rest of the parameters come from readily available archival data.

1.6. *Timeline*

During my time at the University of Wyoming, I have had the privilege of having access to state-of-the-art observatories. This has allowed to collect a lot of data on this project already. Not only that, but because of this access, I have been able to develop my skills in analyzing my data. I have developed my fitting routine, introduced in Section 1.4.3. As such, because of the opportunities afforded to me by the department, I have a lot of the tools and data needed to answer the main questions this project sets out to answer: Can we use bowshock nebulae to measure mass-loss and how does this method compare to others? Given the work I have already conducted, here is a tentative timeline of how I intend to spend the rest of my time here and what papers I envision coming from this work.

1.6.1. *Paper I: Stellar parameters of central bowshock stars*

This paper will compile spectroscopic observations serving as a census of bowshock stars. This paper will present the results of analyzing the spectra of 120 stars central to bowshock nebulae and extract the stellar parameters from optical blue spectra using the code Bayesian-sampler and spectroscopic fitting routine mentioned in Section 1.4.3. I expect to submit this paper by the end of Fall 2024.

1.6.2. *Paper II: Comparing mass-loss calculations using 24 μm and 70 μm data*

This paper will attempt to answer whether 24 μm data can be used in-lieu of 70 μm measurements. In previous works (Kobulnicky et al. 2017, 2018), shock fronts were shown to be detectable in 70 μm measurements. Analyzing more bowshocks however revealed a majority of bowshock nebulae did not have 70 μm detections above the background. Interpolating j_ν using 24 μm data could allow access to measuring mass-loss rates to more stars. Limiting to 70 μm could have the benefit of avoiding stochastic heating effects. I expect to submit this paper by Spring 2025.

1.6.3. *Paper III: Mass-loss rates compared by spectral-type*

This paper will examine how mass-loss varies with spectral-type. This is a direct continuation on the work presented in Kobulnicky et al. (2018, 2019), with the use of optical blue spectra. The new spectra used in this work will allow determination of temperatures to a finer precision as was done in previous works and thus, improved sensitivity to the relation between how mass loss varies with temperature, surface-gravity, and possibly rotational velocity. I expect to submit this paper by Spring 2026.

REFERENCES

Abbott, B. P., Abbott, R., Abbott, T. D., et al. 2017a, PhRvL, 119, 161101, doi: 10.1103/PhysRevLett.119.161101

—. 2017b, ApJL, 848, L12, doi: 10.3847/2041-8213/aa91c9

—. 2019, Physical Review X, 9, 031040, doi: 10.1103/PhysRevX.9.031040

Abbott, D. C., Bieging, J. H., Churchwell, E., & Cassinelli, J. P. 1980, ApJ, 238, 196, doi: 10.1086/157973

Acreman, D. M., Stevens, I. R., & Harries, T. J. 2016, MNRAS, 456, 136, doi: 10.1093/mnras/stv2632

Airapetian, V. S., & Usmanov, A. V. 2016, ApJL, 817, L24, doi: 10.3847/2041-8205/817/2/L24

Aschenbrenner, P., Przybilla, N., & Butler, K. 2023, A&A, 671, A36, doi: 10.1051/0004-6361/202244906

Bragança, G. A., Daflon, S., Cunha, K., et al. 2012, AJ, 144, 130, doi: 10.1088/0004-6256/144/5/130

Burssens, S., Simón-Díaz, S., Bowman, D. M., et al. 2020, A&A, 639, A81, doi: 10.1051/0004-6361/202037700

Castor, J. I., Abbott, D. C., & Klein, R. I. 1975, ApJ, 195, 157, doi: 10.1086/153315

Comeron, F., & Kaper, L. 1998, A&A, 338, 273

Crowther, P. A. 2007, ARA&A, 45, 177, doi: 10.1146/annurev.astro.45.051806.110615

Crowther, P. A., Lennon, D. J., & Walborn, N. R. 2006, A&A, 446, 279, doi: 10.1051/0004-6361:20053685

Czekala, I., Andrews, S. M., Mandel, K. S., Hogg, D. W., & Green, G. M. 2015, ApJ, 812, 128, doi: 10.1088/0004-637X/812/2/128

de Almeida, E. S. G., Marcolino, W. L. F., Bouret, J. C., & Pereira, C. B. 2019, A&A, 628, A36, doi: 10.1051/0004-6361/201834266

Dessart, L., & Owocki, S. P. 2005, A&A, 437, 657, doi: 10.1051/0004-6361:20052778

Draine, B. T., & Li, A. 2007, ApJ, 657, 810, doi: 10.1086/511055

Drew, J. E. 1990, ApJ, 357, 573, doi: 10.1086/168945

Eather, R. H. 1980, Majestic lights: the aurora in science, history, and the arts, Vol. 34 (Wiley Online Library)

Elmegreen, B. G., & Lada, C. J. 1977, ApJ, 214, 725, doi: 10.1086/155302

Feldmeier, A. 1995, A&A, 299, 523

Foreman-Mackey, D., Hogg, D. W., Lang, D., & Goodman, J. 2013, Publications of the Astronomical Society of the Pacific, 125, 306–312, doi: 10.1086/670067

Fullerton, A. W., Massa, D. L., & Prinja, R. K. 2006, ApJ, 637, 1025, doi: 10.1086/498560

Garmany, C. D., Olson, G. L., van Steenberg, M. E., & Conti, P. S. 1981, ApJ, 250, 660, doi: 10.1086/159413

Gormaz-Matamala, A. C., Cuadra, J., Meynet, G., & Curé, M. 2023, A&A, 673, A109, doi: 10.1051/0004-6361/202345847

Gormaz-Matamala, A. C., Curé, M., Meynet, G., et al. 2022, A&A, 665, A133, doi: 10.1051/0004-6361/202243959

Gray, R. O., & Corbally, Christopher, J. 2009, Stellar Spectral Classification

Gull, T. R., & Sofia, S. 1979, ApJ, 230, 782, doi: 10.1086/157137

Gvaramadze, V. V., Langer, N., & Mackey, J. 2012, MNRAS, 427, L50, doi: 10.1111/j.1745-3933.2012.01343.x

Gvaramadze, V. V., Menten, K. M., Kniazev, A. Y., et al. 2014a, MNRAS, 437, 843, doi: 10.1093/mnras/stt1943

Gvaramadze, V. V., Miroshnichenko, A. S., Castro, N., Langer, N., & Zharikov, S. V. 2014b, MNRAS, 437, 2761, doi: 10.1093/mnras/stt2087

Gvaramadze, V. V., Röser, S., Scholz, R. D., & Schilbach, E. 2011, A&A, 529, A14, doi: 10.1051/0004-6361/201016256

Gvaramadze, V. V., Fabrika, S., Hamann, W. R., et al. 2009, MNRAS, 400, 524, doi: 10.1111/j.1365-2966.2009.15492.x

Hainich, R., Ramachandran, V., Shenar, T., et al. 2019, A&A, 621, A85, doi: 10.1051/0004-6361/201833787

Hamann, W. R. 1981, A&A, 93, 353

Hartigan, P., Raymond, J., & Hartmann, L. 1987, ApJ, 316, 323, doi: 10.1086/165204

Helfand, D. J., Gotthelf, E. V., & Halpern, J. P. 2001, ApJ, 556, 380, doi: 10.1086/321533

Holgado, G., Simón-Díaz, S., Herrero, A., & Barbá, R. H. 2022, A&A, 665, A150, doi: 10.1051/0004-6361/202243851

Howarth, I. D., & Prinja, R. K. 1989, ApJS, 69, 527, doi: 10.1086/191321
Huang, W., Gies, D. R., & McSwain, M. V. 2010, ApJ, 722, 605, doi: 10.1088/0004-637X/722/1/605
Huenemoerder, D. P., Oskinova, L. M., Ignace, R., et al. 2012, ApJL, 756, L34, doi: 10.1088/2041-8205/756/2/L34
Humphreys, R. M., & Davidson, K. 1994, PASP, 106, 1025, doi: 10.1086/133478
Irrgang, A., Przybilla, N., Heber, U., et al. 2014, A&A, 565, A63, doi: 10.1051/0004-6361/201323167
Jayasinghe, T., Dixon, D., Povich, M. S., et al. 2019, MNRAS, 488, 1141, doi: 10.1093/mnras/stz1738
Klein, R. I., & Castor, J. I. 1978, ApJ, 220, 902, doi: 10.1086/155980
Kobulnicky, H. A., Chick, W. T., & Povich, M. S. 2018, ApJ, 856, 74, doi: 10.3847/1538-4357/aab3e0
—. 2019, AJ, 158, 73, doi: 10.3847/1538-3881/ab2716
Kobulnicky, H. A., Gilbert, I. J., & Kiminki, D. C. 2010, ApJ, 710, 549, doi: 10.1088/0004-637X/710/1/549
Kobulnicky, H. A., Schurhammer, D. P., Baldwin, D. J., et al. 2017, AJ, 154, 201, doi: 10.3847/1538-3881/aa90ba
Kobulnicky, H. A., Chick, W. T., Schurhammer, D. P., et al. 2016, ApJS, 227, 18, doi: 10.3847/0067-0049/227/2/18
Kounkel, M., Covey, K., Moe, M., et al. 2019, AJ, 157, 196, doi: 10.3847/1538-3881/ab13b1
Kraft, R. P. 1967, ApJ, 150, 551, doi: 10.1086/149359
Krtička, J. 2014, A&A, 564, A70, doi: 10.1051/0004-6361/201321980
Kudritzki, R.-P., & Puls, J. 2000, ARA&A, 38, 613, doi: 10.1146/annurev.astro.38.1.613
Lamers, H. J. G. L. M., Cerruti-Sola, M., & Perinotto, M. 1987, ApJ, 314, 726, doi: 10.1086/165100
Lamers, H. J. G. L. M., & Leitherer, C. 1993, ApJ, 412, 771, doi: 10.1086/172960
Lamers, H. J. G. L. M., Snow, T. P., & Lindholm, D. M. 1995, ApJ, 455, 269, doi: 10.1086/176575
Landau, L. D., & Lifshitz, E. M. 1987, Fluid Mechanics
Lanz, T., & Hubeny, I. 2003, ApJS, 146, 417, doi: 10.1086/374373
—. 2007, ApJS, 169, 83, doi: 10.1086/511270
Leitherer, C. 1988, ApJ, 326, 356, doi: 10.1086/166097
Lucy, L. B. 2010, A&A, 512, A33, doi: 10.1051/0004-6361/200913400
Marcolino, W. L. F., Bouret, J. C., Martins, F., et al. 2009, A&A, 498, 837, doi: 10.1051/0004-6361/200811289
Markova, N., Puls, J., Repolust, T., & Markov, H. 2004, A&A, 413, 693, doi: 10.1051/0004-6361:20031463
Martini, P., Stoll, R., Derwent, M. A., et al. 2011, PASP, 123, 187, doi: 10.1086/658357
Martins, F., Schaerer, D., Hillier, D. J., et al. 2005, A&A, 441, 735, doi: 10.1051/0004-6361:20052927
Mathis, J. S., Mezger, P. G., & Panagia, N. 1983, A&A, 128, 212
Meynet, G., Maeder, A., Schaller, G., Schaerer, D., & Charbonnel, C. 1994, A&AS, 103, 97
Milne, E. A. 1926, MNRAS, 86, 459, doi: 10.1093/mnras/86.7.459
Mokiem, M. R., de Koter, A., Vink, J. S., et al. 2007, A&A, 473, 603, doi: 10.1051/0004-6361:20077545
Mugnes, J. M., & Robert, C. 2015, MNRAS, 454, 28, doi: 10.1093/mnras/stv1889
Noriega-Crespo, A., van Buren, D., & Dgani, R. 1997a, AJ, 113, 780, doi: 10.1086/118298
—. 1997b, AJ, 113, 780, doi: 10.1086/118298
Owocki, S. P., Castor, J. I., & Rybicki, G. B. 1988, ApJ, 335, 914, doi: 10.1086/166977
Panagia, N., & Felli, M. 1975, A&A, 39, 1
Pauldrach, A. W. A., Kudritzki, R. P., Puls, J., & Butler, K. 1990, A&A, 228, 125
Peri, C. S., Benaglia, P., & Isequilla, N. L. 2015, A&A, 578, A45, doi: 10.1051/0004-6361/201424676
Plaskett, H. H. 1922, JRASC, 16, 137
Puls, J., Owocki, S. P., & Fullerton, A. W. 1993, A&A, 279, 457
Puls, J., Vink, J. S., & Najarro, F. 2008, A&A Rv, 16, 209, doi: 10.1007/s00159-008-0015-8
Puls, J., Kudritzki, R. P., Herrero, A., et al. 1996, A&A, 305, 171
Repolust, T., Puls, J., & Herrero, A. 2004, A&A, 415, 349, doi: 10.1051/0004-6361:20034594

Schatzman, E. 1962, Annales d'Astrophysique, 25, 18
Simón-Díaz, S. 2020, in Reviews in Frontiers of Modern Astrophysics; From Space Debris to Cosmology, 155–187, doi: 10.1007/978-3-030-38509-5_6
Simón-Díaz, S., Godart, M., Castro, N., et al. 2017, A&A, 597, A22, doi: 10.1051/0004-6361/201628541
Simón-Díaz, S., & Herrero, A. 2014, A&A, 562, A135, doi: 10.1051/0004-6361/201322758
Sundqvist, J. O., Puls, J., Feldmeier, A., & Owocki, S. P. 2011, A&A, 528, A64, doi: 10.1051/0004-6361/201015771
van Buren, D., & McCray, R. 1988, ApJL, 329, L93, doi: 10.1086/185184
van Buren, D., Noriega-Crespo, A., & Dgani, R. 1995, AJ, 110, 2914, doi: 10.1086/117739
van der Kruit, P. C., & Freeman, K. C. 2011, ARA&A, 49, 301, doi: 10.1146/annurev-astro-083109-153241
Vassiliadis, E., & Wood, P. R. 1993, ApJ, 413, 641, doi: 10.1086/173033
Vink, J. S., de Koter, A., & Lamers, H. J. G. L. M. 2001, A&A, 369, 574, doi: 10.1051/0004-6361:20010127
Wang, Z., Kaplan, D. L., Slane, P., Morrell, N., & Kaspi, V. M. 2013, ApJ, 769, 122, doi: 10.1088/0004-637X/769/2/122
Weßmayer, D., Przybilla, N., & Butler, K. 2022, A&A, 668, A92, doi: 10.1051/0004-6361/202243973
Willson, L. A. 2000, ARA&A, 38, 573, doi: 10.1146/annurev.astro.38.1.573
Wright, A. E., & Barlow, M. J. 1975, MNRAS, 170, 41, doi: 10.1093/mnras/170.1.41